Effect of helium, strontium and silver implanted into silicon carbide on the structural changes and migration of the implants

by

Gcobani Ntshobeni

Submitted in partial fulfilment of the requirements for the degree

Master of Science (MSc) in Physics

In the Faculty of Natural and Agricultural Science

University of Pretoria

March 2022

Supervisor: Prof T.T. Hlatshwayo

Co-Supervisor: Dr M Mlambo

DECLARATION OF ORIGINALITY

I, Gcobani Ntshobeni declare that the dissertation, which I hereby submit for the degree of MSc in Physics at the University of Pretoria, is my own work and has not previously been submitted by me for a degree at this or any other tertiary university.

Signature …….

Date …….

SUMMARY

Containment of radioactive fission products (FPS) is a cornerstone in the revival of nuclear reactors as a clean energy source. In modern generation IV nuclear reactors, safety is enhanced by coating the fuel kernel with four layers of chemical vapour deposited carbon and silicon carbide (SiC). The coated fuel is known as the tri-structural isotropic (TRISO) particle. In this coated particle, silicon carbide (SiC) is the main barrier for radioactive fission products. TRISO particle retains quite well majority of the fission products with exception of some radioactive FPs such as silver (Ag) and strontium (Sr). The release of radioactive FPs poses significant danger to humans and the environment. Several investigations have been conducted on the migration behaviour of Ag and Sr ions in SiC at high temperatures mimicking the operating and accident conditions. Even though, FPs co-exist in the presence of helium (He), the role of He ions in the migration of different FPs in SiC has not been thoroughly investigated. He ions are known to form bubbles in SiC, which can greatly affect the effectiveness of SiC as the main barrier of FPs. Hence, its role in the migration of important fission products needs to be investigated.

In this study, the effect of helium (He), strontium (Sr) and silver (Ag) ions implantation into silicon carbide (SiC) on the structural changes and migration of the implants was investigated. Ag ions of 360 keV were implanted into polycrystalline SiC to a fluence of 2×10^{16} cm^{-2} at 600 ^{o}C. On the same samples, Sr ions of 280 keV were also implanted to a fluence of 2×10^{16} cm^{-2} at 600 ^{o}C (Ag&Sr-SiC). Some of the co-implanted samples were then implanted with 17 keV He ions to a fluence of 1×10^{17} cm^{-2} at 350 ^{o}C (Ag&Sr&He-SiC). The as-implanted samples were then isochronally annealed at temperatures ranging from 1000 ^{o}C to 1300 ^{o}C in steps of 100 ^{o}C for 5 hours. The as-implanted and annealed samples were characterized by Raman spectroscopy, scanning electron microscopy (SEM), atomic force microscopy (AFM), elastic recoil detection analysis (ERDA) and Rutherford backscattering spectroscopy (RBS).

In both the Ag&Sr-SiC and Ag&Sr&He-SiC samples, implantations retained some defects without amorphization of SiC structure. Annealing caused progressive removal of defects in both implanted samples. Co-implantation of He ions resulted in the formation of blisters and holes on the surface. The formation blisters and holes were the results of He bubbles in the implanted region and high He ions implantation temperature which resulted in the some out diffusion of He leaving holes or cavities in the implanted region. The exfoliation of the surface increased with increasing annealing temperature resulting in more holes on the surface.

Annealing the Ag&Sr-SiC and Ag&Sr&He-SiC samples at 1000 ^{o}C caused the migration of implanted Ag ions and Sr ions towards the bulk and the surface in the annealed Ag&Sr&He-SiC samples indicating some trapping in cavities. Since the migration of implanted species was not seen in the Ag&Sr-SiC samples annealed at 1000 ^{o}C, He bubbles enhance some migration while cavities trap the implanted species.

ACKNOWLEDGEMENTS

It is with deep gratitude and appreciation that I extend my sincere thanks and appreciation to my supervisor Prof T.T. Hlatshwayo as well as to my co-supervisor Dr. M Mlambo, for their continuous support of my master's degree, for their patience, motivation and immense knowledge. Their guidance and advice carried me through all the stages of writing of my project. Furthermore, I would like to thank Dr Z.A.Y. Abdalla, Mr T.F. Mokgadi and Miss S.Z. Mtsi for their support and assistance, not forgetting all my fellow students for their many helpful discussions and insightful ideas during the course of this project and the nuclear materials group and friends are also appreciated for their support and encouragement.

As well, I would like to give special thanks to my family for the continuous support and understanding offered to me as I pursued my research and writing project. I have survived so far because of your prayers.

I am extremely grateful for the National Research Foundation (NRF) funding I received during my studies.

Finally, I would like to express my gratitude to God, I am thankful that you have been there for me during all of my trials. Your guidance has become more evident to me every day. It is because of you that I was able to complete my master's degree. Regardless of what happens in the future, I will keep on trusting you.

Table of contents

List of Figures

Chapter 1

Introduction

1.1 Background

The growing concerns of global warming and climate change have bad impacts on economic growth and environmental pollution [1]. The burning of fossil fuels such as oil, coal and natural gas to produce electricity is a main contributor to global warming. This is due to a large amount of carbon dioxide that is produce during the burning of fossil fuels. Carbon dioxide is one of the greenhouse gases that contribute to the increase in global warming and climate change. Therefore, to alleviate global warming, an alternative method of generating electricity that produces a low level of carbon dioxide needs to be considered.

Renewable and non-renewable energy sources are the methods used in generating electricity. Renewable energy source consists of wind energy, solar energy, hydroelectric energy, geothermal energy and biomass. Non-renewable energy includes fossil fuels and nuclear power. With wind energy, energy from the wind is used to generate electricity. The problem with wind is that if the wind is blowing too hard or there is no wind, the wind turbine will not be able to generate sufficient electricity. Solar energy uses energy from the sun to produce electricity, however, on a cloudy day or in a rainy day, the amount of electricity that is produced might not be sufficient. Hydropower uses water from a large reservoir, the water flows through a turbine that turns it, allowing the generator to generate electricity. During the dry season, when no water flows into a larger reservoir, no electricity is generated. Geothermal energy uses heat from the earth's subsurface, where water or steam carries geothermal energy to the earth's surface. As a means of producing energy, geothermal energy poses an environmental concern that result from greenhouse gas emissions. Biomass energy is the energy generated by a living organism or an organism that once lived. The materials commonly used in biomass to generate electricity are plants, wood and waste. When produced, biomass energy generates carbon dioxide, which is one of the greenhouse gases that contribute to the increase of climate change. Fossil fuel and nuclear power are non-renewable energy sources. In fossil fuel, coal, oil and natural gas are burnt to produce heat, the heat is then used to boil water to produce steam that drives turbines to generate electricity. This process of burning fossil fuels generates a large amount of carbon dioxide which contributes to climate change.

Despite the fact that each form of electricity generation has its virtues and shortcomings, long-term electricity generation should be associated with low levels of greenhouse gas emissions. Creating electricity from nuclear energy is an alternative source of electricity supply that is safe, reliable, and environmentally friendly. It produces electricity without emitting any carbon dioxide during operation and uses nuclear fission instead of burning fossil fuels to produce energy. As compared to renewable energy or fossil fuels, nuclear power generates electricity at a higher capacity. The capacity factor is determined based on the amount of electricity generated. Nuclear energy is a key for building a clean energy future that is sustainable and affordable. Using nuclear energy, we can lessen our impact on the environment, maintain clean air, and reliably produce clean, plentiful energy for all. Moreover, nuclear energy is cheap, baseload, dispatchable, and reliable for about six decades. The only main concern of nuclear reactors is safety, which might be caused by the release of radiological fission products (FPs). In modern nuclear reactors, the safety is achieved by coating the fuel particles with chemical vapour deposited (CVD) layers [2]. Fig 1.1 shows the schematic representation of a typical coated particle [3]. The fuel particle consists of kernel of uranium oxycarbide (UCO) or uranium oxide (UO_2) that are then coated by four chemical vapour deposited layers [4]. These layers are porous carbon buffer which is designed to reduce recoiling fission products and accommodate internal gas build-up. Inner pyrolytic carbon (IPyC) acts as a barrier to most non-metallic fission products and gaseous fission products. Silicon carbide (SiC) acts as the main diffusion barrier to prevent the release of fission products (FPs). Outer pyrolytic carbon (OPyC) protects silicon carbide. This coated particle is known as a tri-isotropic (TRISO) particle [5]. This particle is the most promising structural material for manufacturing fuels that provide improvements in quality, repeatability or cost.

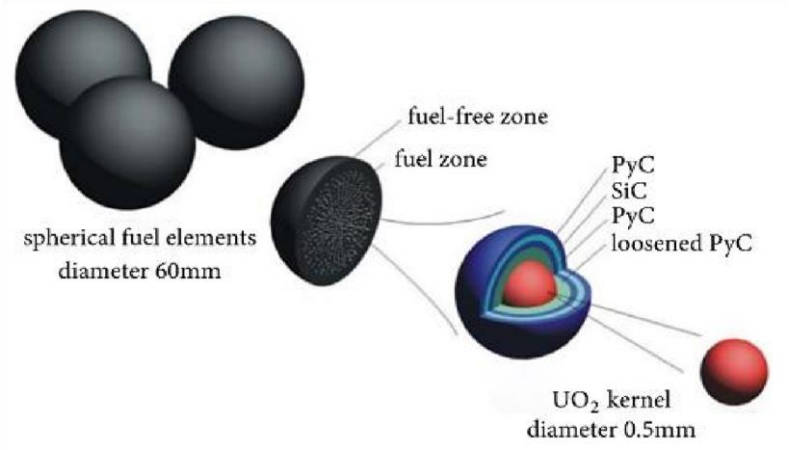

Figure 1. 1: *The schematic representation of the TRISO fuel particle. Taken from [6].*

1.2 Silicon carbide (SiC): Structure and properties

Silicon carbide is considered as one of the few lightweight covalently bonded ceramics with interesting properties. These properties include high thermal conductivity, high thermal stability, chemical inertness, high hardness, low neutron cross section, mechanical stability, and high resistance to radiation damage, oxidation and corrosion [7]. The outstanding properties of SiC make it the best candidate for high temperature applications, specifically in the nuclear industries [8]. As mentioned earlier, SiC is used as a main barrier to prevent the release of fission products and to provide structural support in TRISO fuel particles [9]. SiC compound consists of silicon (Si) atom and four carbon (C) atoms, which are covalently bonded. In the SiC compound either Si is bonded to four C or C bonded to four Si to form very strong tetrahedral covalent bonds, as shown in Fig. 1.2. SiC has more than 200 polytypes depending on the stacking sequence [10]. The stacking sequence of the various polytypes can be expressed in terms of the familiar notations A, B and C, as shown in Fig. 1.3. The most common SiC polytypes are cubic SiC (3C-SiC), hexagonal SiC (4H-SiC and 6H-SiC), and rhombohedral SiC (15R-SiC) [11]. Referring to the properties of SiC mentioned earlier, the hardness of SiC is due to a high bond strength resulting from the short bond between Si and C which is 1.89 Å [12]. The high resistance of SiC against corrosion is due to the strong chemical bond energy, i.e. the cohesive energy per atom of SiC is 6.34 eV. [13, 14]. Since SiC decomposes in a vacuum at about 1700 °C, it has the ability to retain most of these extraordinary properties. The most preferred SiC that is used for a high-temperature nuclear reactor is 3C-SiC because of its high radiation resistance against neutron bombardment [15].

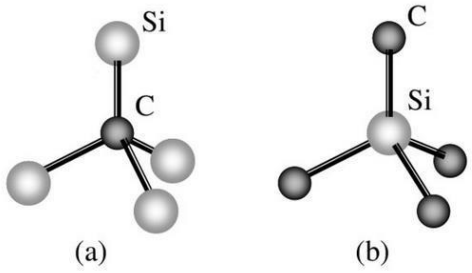

Figure 1. 2: *Basic elements of SiC crystals: Tetrahedrons containing (a) one C and four Si (b) one Si and four C atoms. Taken from [16].*

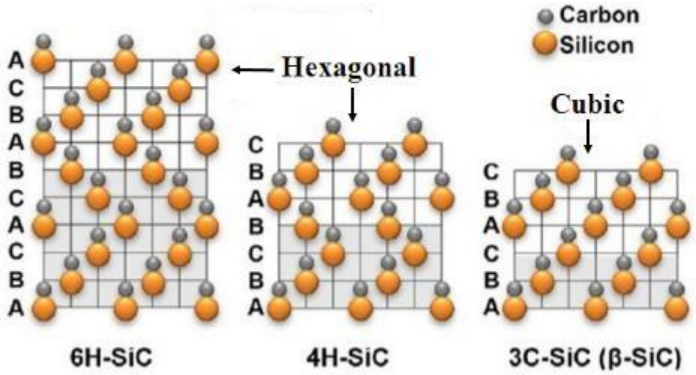

Figure 1. 3: *The stacking sequence of three most commonly SiC polytypes, 6H-, 4H-and 3CSiC. Taken from [17].*

1.3 Performance of TRISO particle

During nuclear fission process in a core of the fuel kernel, unstable nuclei splits into two fission products (FPS) while releasing 2 or 3 neutrons and a lot of energy [18]. Some of the released FPs are unstable or radioactive nuclei and may emit gamma radiation, beta or alpha, or even neutrons, depending on the type of radioactive decay involved, i.e. the manner in which the resulting new nuclei become more stable [19]. All these radiation types have harmful effects on the environment depending on the intensity of ionizing radiation [19]. In a TRISO particle, alpha particles are produced, causing materials to swell and embrittlement [20]. An alpha particle is structurally equivalent to the nucleus of a helium ions (He) atom, consists of two protons and two neutrons. In a nuclear reactor environment, helium accumulation results from the emission of α-particles from nuclear reactions as well as helium infusion from the coolant [15]. Since He has a very low solubility in most solids, it tends to cluster and form bubbles [21]. These bubbles can induce detrimental modifications of the material's structure and mechanical properties [21]. Some studies have reported the effects of He ions on the microstructural and mechanical properties changes of SiC [16-18, 20-22]. It has also been reported that helium-vacancy clusters form bubbles upon annealing, which causes the properties of SiC to deteriorate [22-24]. Thus, He bubbles may cause SiC to lose its legitimacy as the main diffusion barrier for the fission products in the TRISO coated fuel particles.

Under the operation conditions, the TRISO particle retains most of the important fission products with the exception of some like silver (^{110m}Ag), strontium (Sr) ions [25]. ^{110m}Ag ions are strong gamma emitter with a half-life of 250 days [26]. Hence, if released, it can cause danger to personnel and environment. ^{90}Sr is a radioactive isotope of strontium ions produced by nuclear fission. ^{90}Sr ions are one of the most important fission products due to its relatively high yield and uptake and retention in the biological system [27]. It is a beta emitter with a half-

life of 28.6 years [28]. The release of strontium ions into the environment could cause health hazard [29]. It can be deposited in the bones and replace calcium and can cause cancer of the bones [30, 31]. For these reasons, silver and strontium are products of fission that deserve more attention.

1.4 Previous studies of Ag and Sr ions migration behaviour in SiC

In recent years, extensive work has been carried out to understand the migration behaviour of Ag and Sr ions in SiC in temperatures ranging from the temperature of the nuclear reactor during normal operating and accident conditions.

A study by E. Friedland *et al*. [32] investigated the diffusion of Ag in 6H-SiC and CVD-SiC. In that study, 360 keV Ag^+ with a fluence of 2×10^{16} cm^{-2} were implanted at room temperature, at 350 °C and 600 °C. The authors found that silver implanted at room temperature amorphized the near-surface region of SiC but those implanted above 350 °C retain the crystalline structure. In that study, the diffusion and loss of Ag during vacuum annealing at temperatures up to 1600 °C were determined. They found that strong Ag ions diffusion occurred after annealing at 1300 °C in both 6H-SiC and CVD-SiC. This is mainly attributed to the radiation damage caused by the implant. No additional diffusion was observed in the 6H-SiC samples after further annealing at this temperature for 80 hours, while it was significantly reduced in CVD-SiC. They attributed the diffusion in CVD-SiC to grain boundary diffusion. A study by Abdelbagi *et al.* [33] investigated migration behaviour of Sr in polycrystalline SiC.

In this study, SiC samples were implanted with 360 keV Sr^+ ions to a fluence of 2×10^{16} cm^{-2}. The implanted samples were isochronal annealed in vacuum at temperatures ranging from 1100 to 1500 °C in steps of 100 °C for 5 h. Implantation of Ag ions amorphized the near-surface region of the SiC substrate. Annealing at 1100 °C resulted in the recrystallization of the amorphous SiC. At this temperature, a strong migration of Sr towards the surface was observed. This was accompanied by significant loss of implanted Sr ions. Annealing at higher temperature (1500 °C) led to the decomposition of SiC, and samples retained about 25% of Sr ions. This loss was due to the presence of pores on the sample surface. A study by Hlatshwayo *et al*. [34] also investigated the effect of Ag and Sr ions implanted into polycrystalline SiC. For comparison purposes, 360 keV Ag^+ and 280 keV Sr^+ ions were individually implanted into SiC. Some of the Ag implanted SiC (Ag-SiC) were then implanted with Sr ions (Ag & Sr-SiC). Both implantations were performed at 600 °C to a fluence of 2×10^{16} cm^{-2}. All implanted SiC were sequentially annealed at temperatures ranging from 1000 to 1400 °C in steps of 100 °C for 5 hours. The results showed that Sr ions implantation also led to the formation of Ag precipitate.

Dual implantation (Ag & Sr-SiC) resulted in a higher concentration of defects compared to individual implants (Ag-SiC and Sr-SiC). They reported that the defects in the former were due to the interaction of defects retained by the Ag and Sr ions resulting in more complex defects. Annealing resulted in reduction of defects with slightly pronounced reduction of defects in the Ag&Sr&He-SiC. Annealing also caused the implants to migrate towards the surface. This migration was accompanied by loss at 1400 °C while no loss was observed in the Sr-SiC samples.

The effects of He bubbles on the migration behaviour of Ag ions in polycrystalline SiC was investigated in a recent study by Hlatshwayo *et al.* [35]. In this study, Ag and He ions were co-implanted into SiC at room temperature. The co-implanted samples were then annealed at 1100 °C for 5 h under vacuum. The study reported that implantation led to the formation of nanosized He bubbles in the amorphous SiC layers, and the annealing caused the cavity network to appear mostly parallel to the surface but sometimes branching into the bulk and the surface. Ag migration towards the surface and bulk of SiC was also observed after annealing.

1.5 Research aims and objectives

To fully understand the migration of different fission products (FPs) in SiC, their migration needs to be investigated in the environment mimicking the nuclear environment. In a nuclear reactor, FPs coexist in the presence of He ions. Hence the migration of different FPs in SiC needs to be investigated in the presence of He ions. The aim of this study was to investigate the effect of helium ions, strontium ions and silver ions implanted into silicon carbide on the structural changes and migration of the implants. Ag ions of 360 keV were implanted into polycrystalline SiC to a fluence of 2×10^{16} cm^{-2} at 600 ^{o}C. On the same sample, Sr ions of 280 keV were also implanted to a fluence of 2×10^{16} cm^{-2} at 600 ^{o}C. Some of the co-implanted samples were implanted with 17 keV He ions to a fluence of $1\times10^{17}cm^{-2}$ at a temperature of 350 ^{o}C. The implanted samples were then isochronal annealed at temperatures ranging from 1000 ^{o}C to 1300 ^{o}C in steps of 100 ^{o}C for 5 hours. The as-implanted and annealed samples were then characterized using Raman spectroscopy, scanning electron microscopy (SEM), atomic force microscopy (AFM), elastic recoil detection analysis (ERDA), and Rutherford backscattering spectroscopy (RBS). The results were then compared to identify the role of He bubbles in the migration of Ag ions and Sr ions structural changes and migration of the implants.

1.6 The outlay of this dissertation

The outlay of this dissertation is made up of 7 chapters: Chapter 1 is the introduction. Chapter 2 discusses diffusion theory in solids. Chapter 3 explain ion implantation, chapter 4 analytical techniques are discussed, chapter 5 discussion of experimental procedure. Chapter 6 is the results and discussion. Chapter 7 is the conclusion and future studies.

References

1. Shaw, D. (Ed.). (2012). Atomic diffusion in semiconductors. Springer Science & Business Media.
2. Mathias, M. F., Roth, J., Fleming, J., & Lehnert, W. (2003). Diffusion media materials and characterisation. Handbook of fuel cells fundamentals, technology and applications, 3(Part 1), 517-537.
3. Njoroge, E. G. (2014). Solide-state interaction between Zr thin films and SiC, University of Pretoria,
4. Callister Jr, W. D., & Rethwisch, D. G. (2020). Callister's materials science and engineering. John Wiley & Sons.
5. Crank, J. (1979). The mathematics of diffusion. Oxford university press.
6. Chen, H., Li, C., Xing, H., & Fang, C. (2018). The R&D of HTR-STAC Program Package: Source Term Analysis Codes for Pebble-Bed High-Temperature Gas-Cooled Reactor. Science and Technology of Nuclear Installations.
7. Njoroge, E. G., Theron, C. C., Malherbe, J. B., & Ndwandwe, O. M. (2014). Kinetics of solid-state reactions between zirconium thin film and silicon carbide at elevated temperatures. Nuclear Instruments and Methods in Physics Research Section B: Beam Interactions with Materials and Atoms, 332, 138-142.
8. Snead, L. L., Nozawa, T., Katoh, Y., Byun, T. S., Kondo, S., & Petti, D. A. (2007). Handbook of SiC properties for fuel performance modeling. Journal of nuclear materials, 371(1-3), 329-377.
9. Ivanov, A. M., Strokan, N. B., Davydov, D. V., Savkina, N. S., Lebedev, A. A., Mironov, Y. T., & Ivanov, E. M. (2001). Radiation hardness of SiC based ions detectors for influence of the relative protons. Applied surface science, 184(1-4), 431-436.
10. Matsunami, H. (2004). Technological break throughs in growth control of silicon carbide for high power electronic devices. Japanese Journal of Applied Physics, 43(10R), 6835.
11. Abderrazak, H., & Hmida, E. S. B. H. (2011). Silicon carbide: synthesis and properties. Properties and applications of Silicon Carbide, 361-388.
12. Makhijani, A., & BOYD, M. (2010). Small modular reactors. No solution for the cost, safety, and waste problems of nuclear power. Maryland/Washington: Institute for

    Energy and Environmental Research/Physicians for Social Responsibility

13. Fan, Q., Chai, C., Wei, Q. and Yang, Y., (2016). The mechanical and electronic properties of carbon-rich silicon carbide. Materials, 9(5), p.333.

14. Malherbe, J.B., (2013). Diffusion of fission products and radiation damage in SiC. Journal of Physics D: Applied Physics, 46(47), p.473001.

15. Krautwasser, P., Begun, G. M., & Angelini, P. (1983). Raman spectral characterization of silicon carbide nuclear fuel coatings. Journal of the American Ceramic Society, 66(6), 424-434.

16. Gareiou, Z., Drimili, E., and Zervas, E. (2021). Public acceptance of renewable energy sources. In Low Carbon Energy Technologies in Sustainable Energy Systems (p. 309327). Academic Press.

17. Jian, J. and Sun, J., (2020). A review of recent progress on silicon carbide for photoelectrochemical water splitting. Solar RRL, 4(7), p.2000111.

18. Ahmed, S. N. (2007). Properties and sources of radiation. In Physics and Engineering of Radiation Detection (Second Edition). Elsevier, 1-64.

19. Europe Commission, (2021). Technical assessment of nuclear energy with respect to the do no significant harm criteria of Regulation (EU) 2020/852 (Taxonomy Regulation).

20. Hashimoto, N., Kasada, R., Raj, B., & Vijayalakshmi, M. (2020). Radiation effects in ferritic steels and advanced ferritic-martensitic steels. In Comprehensive Nuclear Materials (Second Edition). Elsevier, 226-254.

21. Trinkaus, H., and Singh, B. N. (2003). Helium accumulation in metals during irradiation–where do we stand? Journal of Nuclear Materials, 323(2-3), 229-242.

22. Zhang, C. H., Donnelly, S. E., Vishnyakov, V. M., & Evans, J. H. (2003). Dose dependence of formation of nanoscale cavities in helium-implanted 4H–SiC. Journal of applied physics, 94(9), 6017-6022.

23. Li, B. S., Zhang, C. H., Zhang, H. H., Shibayama, T., & Yang, Y. T. (2011). Study of the damage produced in 6H-SiC by He irradiation. Vacuum, 86(4), 452-456.

24. Shen, Q., Ran, G., Zhou, W., Ye, C., Feng, Q., & Li, N. (2018). Investigation of surface morphology of 6H-SiC irradiated with He^+ and H_2^+ ions. Materials, 11(2), 282.

25. Internation atomic energy agency, (1997). Fuel performance and fission product behaviour in gas cooled reactors. [online] Available at: http://www.pub.iaea.org/books/IAEABooks/5633/Fuel-Performance-and-Fission Product Behaviour-in Gas Cooled-Reactors [Accessed 8 Feb. 2017].

26. Demkowicz, P., Hunn, J., Morris, R., Harp, J., Winston, P., Baldwin, C., & Rooyen, I. V. (2012). Preliminary results of post-irradiation examination of the AGR-1 TRISO fuel compacts (No. INL/CON-12-24427). Idaho National Lab. (INL), Idaho Falls, ID (United States).

27. Valković, V. Measurements of Radioactivity (2000). Radioactivity in the Environment, 117-258.

28. Danesi, P. R. (2019). Environmental and Health Consequences of Nuclear, Radiological and Depleted Uranium Weapons. Encyclopedia of Environmental Health, 360-376.

29. Petti, D. A., Buongiorno, J., Maki, J. T., Hobbins, R. R., & Miller, G. K. (2003). Key differences in the fabrication, irradiation and high temperature accident testing of US and German TRISO-coated particle fuel, and their implications on fuel performance. Nuclear Engineering and Design, 222(2-3), 281-297.

30. Kołodziejska, B., Stępień, N., & Kolmas, J. (2021). The influence of strontium on bone tissue metabolism and its application in osteoporosis treatment. International Journal of Molecular Sciences, 22(12), 6564.

31. Steinhauser, G., Schauer, V., & Shozugawa, K. (2013). Concentration of strontium-90 at selected hot spots in Japan. PloS one, 8(3), e57760.

32. Friedland, E., Malherbe, J. B., Van der Berg, N. G., Hlatshwayo, T., Botha, A. J., Wendler, E., & Wesch, W. (2009). Study of silver diffusion in silicon carbide. Journal of Nuclear Materials, 389(2), 326-331

33. Abdelbagi, H. A. A., Skuratov, V. A., Motloung, S. V., Njoroge, E. G., Mlambo, M., Hlatshwayo, T. T., & Malherbe, J. B. (2019). Effect of swift heavy ions irradiation on the migration behaviour of strontium implanted into polycrystalline SiC. Nuclear Instruments and Methods in Physics Research Section B: Beam Interactions with Materials and Atoms, 451, 113-121.

34. Hlatshwayo, T. T., Mtshonisi, N., Njoroge, E. G., Mlambo, M., Msimanga, M., Skuratov, V. A., & Motloung, S. V. (2020). Effects of Ag and Sr dual ions implanted into SiC.

Nuclear Instruments and Methods in Physics Research Section B: Beam Interactions with Materials and Atoms, 472, 7-13.

35. Hlatshwayo, T. T., Maepa, C. E., Msimanga, M., Mlambo, M., Njoroge, E. G., Skuratov, V. A., & Malherbe, J. B. (2021). Helium assisted migration of silver implanted into SiC. Vacuum, 183, 109865.

Chapter 2

Diffusion

In this study the migration behaviour of Ag and Sr ions co-implanted into SiC in the presence of He ions was investigated. The migration mechanism of atoms in solids can be via diffusion. Diffusion is a migration mechanism where atoms move from a region of high concentration to a region of low concentration [1]. For atoms to move from their original lattice sites, they need enough energy to overcome the energy barrier between their neighbouring atoms. Hence diffusion is affected by various factors such as structure of the material and temperature [2, 3]. This chapter discussed diffusion.

2.1 Diffusion coefficient

Whenever an atom diffuses in a particulate material, it does so at a certain rate. In a material the diffusion coefficient D describes how fast atoms diffuse. A diffusion coefficient can be determined using Fick's first law:

$$J = -D\frac{dC}{dx} \tag{2.1}$$

Where *J* is the flux (number of atoms diffusing per unit area per second), C is the concentration, which is the number of diffuse particles per unit volume, *dC/dx* is the concentration gradient [4, 5]. The negative in equation 2.1 indicates that diffusion is from a region of higher concentration to a region of lower concentration i.e. opposing the concentration gradient [5].

In most cases, the concentration profile and concentration gradient change over time, and that changes equation 2.1, for determining the diffusion coefficient. The Fick's second law states that the rate of compositional change is equal to diffusivity times the rate of change of the concentration gradient [6]. The Fick's second law describes how concentration profiles change over time. From equation 2.1 diffusion is assumed to be in the x-direction. Then we have:

$$\frac{\mathrm{dC}}{\mathrm{dt}} = -\frac{\mathrm{dJ}}{\mathrm{dx}} \tag{2.2}$$

Concentration and flux are affected by changes in time and position, respectively, but equation 2.2 remains valid at any point in time [7]:

$$\frac{\partial C}{\partial t} = -\frac{\partial}{\partial x}\left(-D\frac{\partial C}{\partial x}\right) \tag{2.3}$$

If the diffusion coefficient D is assumed to be independent of the position, then Fick's second law can be expressed as:

$$\frac{\partial C}{\partial t} = D\frac{\partial^2 C}{\partial x^2} \tag{2.4}$$

In three dimensions, Fick's second law can be written as follows:

$$\frac{dC}{dt} = D\nabla^2 C \qquad 2.5$$

In a limited temperature range, the temperature dependence of the diffusion coefficient obeys Arrhenius dependence and is given by [4]:

$$D = D_o e^{\left(\frac{-E_a}{K_B T}\right)} \qquad 2.6$$

Where D_o is the pre-exponential, E_a is the activation energy, K_B is the Boltzmann constant, T is the absolute temperature in kelvin (K).

2.2 Diffusion Mechanisms

In order for diffusion to occur, it requires an atom to have the energy to break bonds with its neighbours and move to a new location, which may be a defect or an empty space. A crystal may display different types of defects; such as point (vacancies or interstitials) or planar (dislocation loops or stacking faults), complex defects (defects resulting from clustering of point or planar defects). Defect structure plays an important role in the diffusion mechanisms. The major mechanisms of diffusion are discussed in this section. The other mechanisms not discussed in this section are discussed in details elsewhere [8].

2.2.1 Vacancy mechanism

The vacancy in the structure is caused by the absence of an atom from the original lattice site. The missing atom leaves an empty site in the lattice. According to Fig. 2.1, a vacancy is the exchange of an atom from one lattice position to another lattice position. Whenever an atom moves, it moves in the opposite direction of a vacancy (see Fig. 2.1). The movement of an atom from its original lattice site to another lattice site requires sufficient energy to break bonds with its neighbours and create the new lattice position during the movement. The energy required for the vacancy motion is called activation energy. Crystals that are imperfect can show a variety of crystallographic defects. The probability of an atom moving in a solid is given by the product of the probability of finding an electron [9]:

$$N_v = N\ exp\ \left(-\frac{E_v}{K_B T}\right) \qquad 2.7$$

Where the Number of vacancie**s** units per unit volume is N_v , N is the total number of atomic sites, E_v is the energy required to move the atoms from a lattice site within the solid crystal to

the vacancy, K_B is the Boltzmann constant and the absolute temperature in Kelvin is T. In solid crystals, an increase in temperature leads to annealing of defects. This can be seen clearly from equation 2.1.

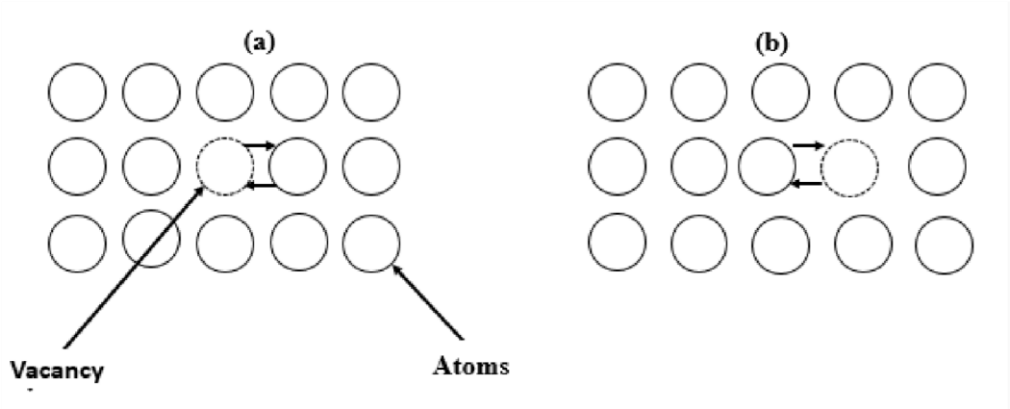

Figure 2. 1: *The schematic representation of vacancy mechanism (a) before and (b) after vacancy diffusion.*

2.2.2 Interstitial diffusion mechanisms

As shown in Fig. 2.2, interstitial diffusion occurs when an atom moves from an interstitial site to an empty site nearby [4]. In some cases, the interstitial atom can be larger or smaller than the host atom. In a solid material, there are more interstitial sites than vacancies, therefore the probability for interstitial diffusion is greater than the probability of vacancy diffusion. The diffusion of small atoms within interstices is faster than the diffusion of vacancies, so the diffusion of interstitial atoms is highly advantageous. Fig. 2.2 shows the region of interstitial diffusion, in which interstitial atoms jump from their interstitial sites to their neighbouring empty sites [4].

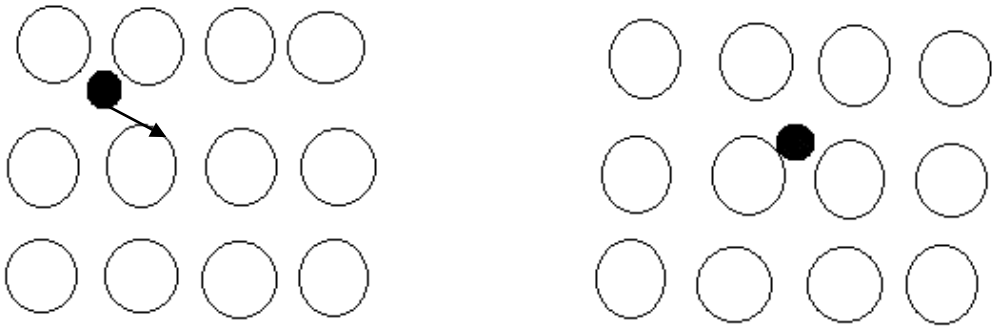

Figure 2. 2: Schematic representation showing a position interstitial atom before diffusing and after diffusion

2.2.3 Interstitialcy Mechanisms

Another diffusion mechanism is known as interstitialcy diffusion. Interstitial atoms in this case have an approximate size of the host atoms. Interstitial atoms can move into another lattice site by pushing their neighbouring lattice atoms out of a lattice position into the lattice site next to them, as shown in Fig. 2.3.

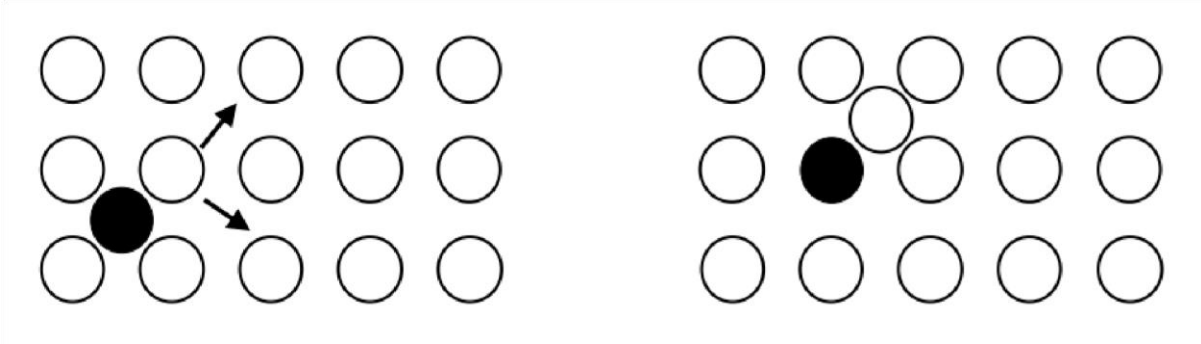

Figure 2. 3: Interstitial mechanism before and after interstitialcy diffusion.

2.3 Grain boundaries and Dislocation

Defects such as dislocations and grain boundaries occur on one and two dimensional surfaces respectively. In both of these defects, the diffusion path is fast. Grain boundaries are found in polycrystalline solids and are interfacial defects between crystallites. The grain boundaries can act as a sink for point defects and a pathway for them to be transported. An extra plane within a lattice structure is usually classified as a dislocation. There are different types of dislocation, including screw, mixed, and edge dislocations. Dislocations result from stresses applied to the matrix, i.e. in an annealed state at high temperatures.

The grain boundaries are thought to occur in two dimensions, and tend to reduce a material's electrical and thermal conductivity. It is more common for corrosion to start along grain boundaries and for precipitation of new phases from the solid at grain boundaries [7]. In addition, grain boundaries play an important role in a number of mechanisms that contribute to creep [10]. A grain boundary disrupts dislocation motion within the material, a common method for enhancing mechanical strength is to reduce the size of crystallites, as described by the Hall–Petch relationship [11]. In materials science, it is important to understand how grain boundaries affect mechanical, electrical, and other properties of materials.

2.4 Diffusion in polycrystalline SiC

A crystalline material is one in which the atoms are situated in a repeating or periodic array over large atomic distances; that is, long-range order exists, such that upon solidification, the atoms

will position themselves in a repetitive three-dimensional pattern, in which each atom is bonded to its nearest-neighbour atoms. A crystalline solid can either be a single crystalline or a polycrystalline. Diffusion is more complicated in polycrystalline materials; this is because diffusion across the grain boundary is difficult to distinguish from diffusion through the volume [12]. This is because diffusing species can also escape from the grain boundary into the lattice. Therefore, diffusion can occur along multiple paths. When the grain boundaries are disordered, diffusion at low temperatures is faster compared to when the grains are intact [8].

2.5 Evaluation of diffusion

There are various methods to evaluate diffusion coefficients in systems as discussed elsewhere [5, 7]. For the diffusion of implanted profiles, most of them rely on comparing the full width at half maximum of the as implanted profiles before and after annealing. In this work the diffusion coefficients were not determined owing to the complex migration behaviour caused by He ions cavities as will be discussed in results and discussion chapter.

Reference

1. Shaw, D. (Ed.). (2012). Atomic diffusion in semiconductors. Springer Science & Business Media.
2. Mathias, M. F., Roth, J., Fleming, J., & Lehnert, W. (2003). Diffusion media materials and characterisation. Handbook of fuel cells—fundamentals, technology and applications, 3(Part 1), 517-537.
3. Njoroge, E. G. (2014). Solide-state interaction between Zr thin films and SiC, University of Pretoria,
4. Callister Jr, W. D., & Rethwisch, D. G. (2020). Callister's materials science and engineering. John Wiley & Sons.
5. Crank, J. (1979). The mathematics of diffusion. Oxford university press.
6. Fick, A. (1855). Ueber diffusion. Annalen der Physik, 170(1), 59-86.
7. Shewmon, P. Diffusion in solid. (1986). the Minerals, Metals and Materials Soc., USA.
8. Heitjans, P. (2005). Diffusion in condensed matter, springer, Netherlands.
9. Heitjans, P., & Kärger, J. (Eds.). (2006). Diffusion in condensed matter: methods, materials, models. Springer Science & Business Media.Shewmon, P. (1989) the Minerals. Metals & Materials Society, Warrendale, PA, 37-38.
10. Raj, R., & Ashby, M. F. (1971). On grain boundary sliding and diffusional creep. Metallurgical transactions, 2(4), 1113-1127.
11. Hansen, N. (2004). Hall–Petch relation and boundary strengthening. Scripta materialia, 51(8), 801-806.
12. Dohmen, R., & Milke, R. (2010). Diffusion in polycrystalline materials: grain boundaries, mathematical models, and experimental data. Reviews in Mineralogy and Geochemistry, 72(1), 921-970.

Chapter 3

Ion implantation

Ion implantation is a process of injecting energetic ions into the surface of a solid to modify its properties or changing the chemical composition of the near-surface. Interactions between injected energetic ions and host atoms cause the injected ions to lose energy until they come to rest inside the material of interest. Ion implantation was used in this study to introduce Ag, Sr and He into SiC. This chapter discusses all the processes taking place until the injected energetic ions come to rest in the substrate.

3.1 Stopping power

The energetic ions impinging a target material interact with atoms of the target material and lose their energy until they come to rest inside material. The amount of energy loss determines how deep they will come to rest inside material and the amount of disorder created in the lattice [1]. The ions are accelerated toward the target with a particular energy, usually from few keV to MeV. These ions lose energy as they are penetrating material, hence the energy loss is function of depth *x*. The stopping power (S) is the average energy loss per unit path length of the particle due to its interaction with the target atom and is given by [2]:

$$S = \frac{dE}{dx} \tag{3.1}$$

The penetrating ions lose their energy via two distinct, independent processes, namely nuclear stopping and electronic stopping. In nuclear stopping, the injected ions lose energy in the material's atoms as a result of elastic collisions between the injected ions and the atoms [3]. In electronic stopping, the energy is lost as a result of an inelastic collision between the impinging ions and the electrons of the atom target [4]. Hence, the total stopping power is the sum of the two stopping powers [2]:

$$S = \left(\frac{dE}{dx}\right)_n + \left(\frac{dE}{dx}\right)_e \tag{3.2}$$

where subscript n and e indicate nuclear and electronic stopping, respectively. Considering the density (*N*) of the target material, one can get the total stopping cross-section by dividing equation (3.1) by the density N, we can find the stopping cross-section as:

$$\varepsilon = -\frac{1}{N}\left(\frac{dE}{dx}\right) = -\frac{1}{N}\left(\frac{dE}{dx}\right)_n - \frac{1}{N}\left(\frac{dE}{dx}\right)_e \quad = \varepsilon_n + \varepsilon e \tag{3.3}$$

where ε_n and ε_e are the nuclear and electron-stopping cross-section, respectively, and the negative sign indicates that dE is less than zero (dE<0)

Fig. 3.1 shows stopping power as a function of ion velocity. There are three regions indicated in Fig. 3.1 i.e. the low, intermediate and high energies regions and they are assigned based on comparing the ion velocity v_i with $v_0 Z_1^{2/3}$, where v_0 is Bohr velocity and Z_1 is the atomic number of an ion. At low energy region ($v_i < v_0 Z_1^{2/3}$) nuclear stopping dominates, at intermediate energy region ($v_i \approx V_0 Z_1^{2/3}$) the electronic stopping dominates, and high energy region ($v_i >> v_0 Z_1^{2/3}$), electronic stopping decreases [5, 6].

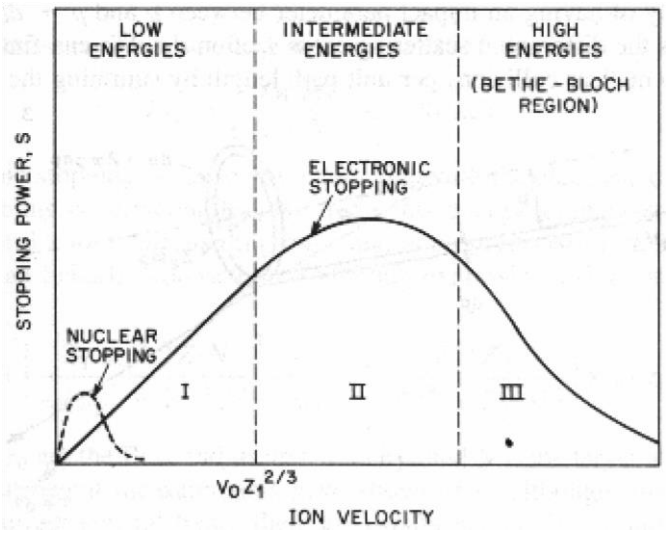

Figure 3. 1: *A representation of stopping power as a function of ion velocity (kinetic energy). Taken from [7].*

3.1.1 Nuclear stopping

Nuclear stopping occurs when energetic ions lose their energy via their interactions with target atoms. During this process the energy of ions is transferred to target atoms. If the energy transferred to the target atoms is greater than their displacement energies the target atoms will be displaced resulting in the formation of lattice disorder such as vacancies and interstitials. In nuclear stopping, the positive charge of an energetic ion is coulomb repelled by the positive cores of the target atom during their interaction and their interatomic potential given by [2]:

$$V = \frac{e^2 Z_1 Z_2}{4\pi\varepsilon r}\phi\left\{\frac{a}{r}\right\} \quad 3.4$$

where Z_1 and Z_2 is the atomic number of the implanted ions and the target atoms respectively, e is the electron charge, r is the distance between an ion of Z_1 and atom of Z_2, is the permittivity of free space and $\phi\left\{\frac{a}{r}\right\}$is the screening function that depends on the electron density distribution in the two atoms.

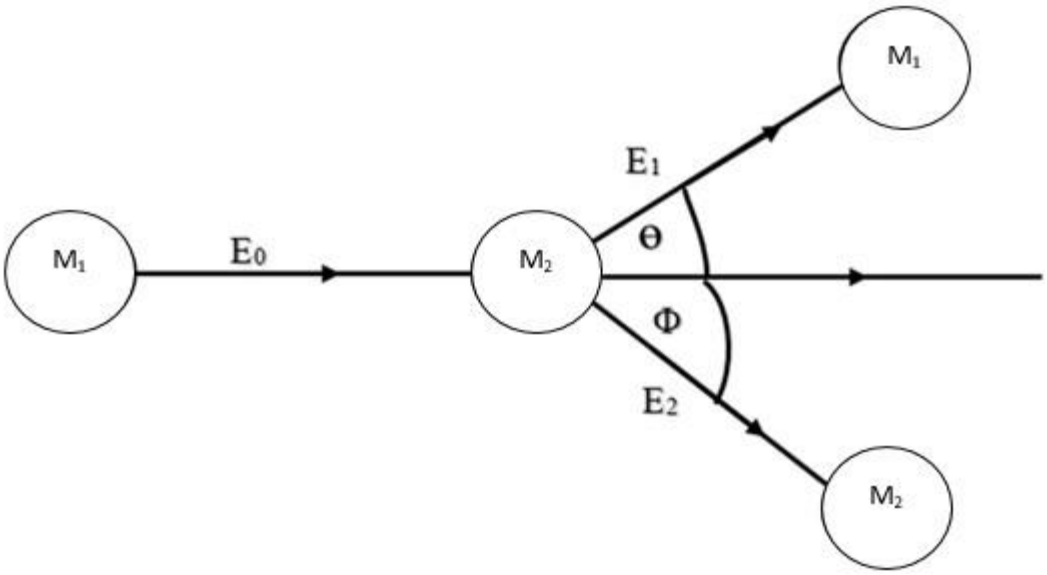

Figure 3. 2: *The diagram of an elastic collision between an energetic ion of mass* ***M_1*** *and stationery target atom of mass* ***M_2****.*

Fig. 3.2 is schematic of a collision between an energetic ion and stationery target atom. When the implanted ion of mass M_1 with a velocity v_o collides with the target atom of mass M_2, energy T is transferred from the energetic ion into the target atom as a result of elastic collision. Using the conservation of momentum and energy, the energy transferred has been found, in the center of mass system:

$$T = E_0 \frac{M_1 M_2}{(M_1+M_2)}\mathrm{Sin}\frac{\theta}{2} = T_{max}\, sin^2\frac{\theta}{2} \quad 3.5$$

where $M_1$is ion's mass, M_2 is the mass of the target atom, E_0 is the ion's initial energy and θ is the scattering angle ɵ in the center of the mass system. From equation 3.5, it is evident that, the maximum transferred will be transferred if θ is 180°.

3.1.2 Electronic stopping

Electron stopping occurs when an impinging energetic ion interacts with electrons of the target atoms and loses energy in the process [5]. This inelastic energy loss is dominant in the second

and third regions divided based of Bohr velocity ($\frac{e}{\hbar}$) [6], as explained earlier, where e is the electron charge and $\hbar$ is plank's constant.

The stopping of electrons in the low-energy region under the assumption of a free electron density is given by ρ [8]:

$$S_e = \int (v, p)\,(Z_1(v))^2\,\rho dV \qquad 3.6$$

where S_e is the electronic stopping, L is the stopping interaction function of the particle (ion) of a unit charge with velocity v, Z_1 is the atomic number of the incident ion, and ρ is the electron density of each volume element of the target dV.

In the region of intermediate energy, the ion velocity is the same as $v_0 Z^{2/3}$ and the ion is fully ionized resulting in the electronic stopping reaching maximum. In the high energy region, the electronic stopping is proportional to z_1^2 according to Bethe-Bloch's equation [9]:

$$\varepsilon_e = \frac{4\Theta^4 \pi Z_2 Z_1^2}{m_e v_1^2}\left[Ln\ \frac{2m_e v_1^2}{I} - Ln(1-\beta^2) - \beta^2 - \frac{c}{z_2} - \frac{\delta}{2}\right] \qquad 3.7$$

where m_e is the mass of the electron, v_1 is the velocity of the projectile, the velocity of the projectile divided by the speed of light is β, (β = v/c), and I is the mean excitation potential given by [10].

3.1.3 Energy loss in a compound

Ions were co-implanted into SiC in this study. Hence, understanding the energy loss in compound is vital. This section discusses the energy loss in a compound. The stopping cross-section for the compound $A_m\ B_n$ is made up of two different elements A and B which is given by:

$$AmBm = m^{A} + n^{B} \qquad 3.8$$

where ^{A} and ^{B} are the stopping power cross-section of elements A and B respectively. The equation is called Bragg's rule [8].

3.1.4 Energy straggling

As the energetic ion is penetrating a substrate, it loses its energy to interaction with the target's atoms, which ultimately leads to energy spread known as energy straggling. Since the interaction of ion with matter is statistically in nature, ions with the same initial energy encounter different interactions resulting in them having different energies after passing through the same target of thickness *x* [11].

In electronic stopping, the energy straggling observed can be deduced from Beth-Bloch equation given below:

$$\Omega_B^2 = 4\pi Z_1^2 Z_2 e^4 N\Delta x \qquad 3.9$$

where Ω_B^2 is the energy loss of a projectile after passing through a target thickness *x*, Z_1 and Z_2 are the atomic number of ion and target atom respectively, *N* is the area density of the target and e is the electron charge. The distribution of the energy which emerges from independent collisions is approximately Gaussian when the energy loss is smaller than the incident energy [11]. Therefore, the full width at maximum (FWHM) of loss of energy distribution is given as:

$$\mathrm{FWHM_B} = 2\Omega_B\sqrt{2ln2} \qquad 3.10$$

where Ω_B is the standard deviation. Lindhard *et al* [12] extended the Bohr Theory of straggling to include energy correction where the assumption may not be correct. In a target compound, the sum of energy straggling is said to be linear additivity rule similar to the Bragg's rule [13].

3.1.5 Range and Range Straggling

In a material, an energetic ion loses energy through nuclear and electronic stopping. In general, implantation doses are typically higher than 10^{12} ions/cm^2 and using statistical means, it is possible to predict ion trajectory [14]. The range R refers to the total average path length. It is mainly composed of lateral and vertical movements. As a result of implanting ions, the average depth of the ions is known as the projected range, Rp, and the distribution of the implanted ions

about that depth can be assumed to be Gaussian with a standard deviation δp (ΔRp). The range can be calculated from the stopping cross-section [15]:

$$R = \int_0^E \frac{dE}{-dE/dx} \qquad 3.11$$

Since electronic stopping is more dominant at high energies, an energetic ion path is initially a straight line. As the ion energy decrease the path becomes zigzag towing to nuclear stopping that is dominant at low energies. Fig. 3.3 shows a typical path of an ion takes penetrating the target material.

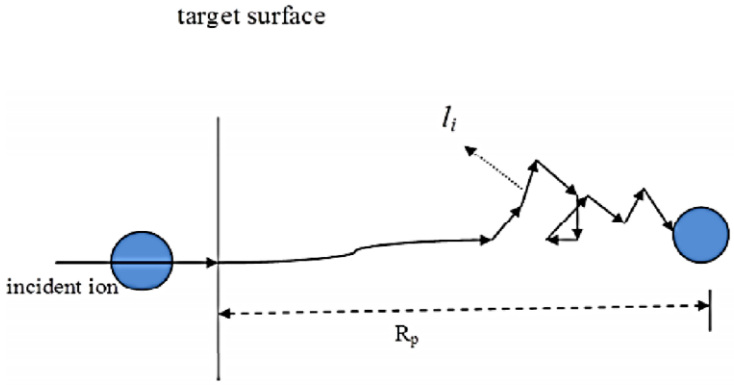

Figure 3. 3: *Schematic diagram showing energetic ion travelling inside the material.*

Fig. 3.3 shows an ion traveling through a material until it comes to rest within the material. The lateral motion of ions may limit dimensions in some devices [15]. Ion concentration profiles in solids are related to projected range, Rp, standard deviation ΔRp and ion fluence (ϕ), by Gaussian approximation:

$$\mathrm{N}(x) = \frac{\phi}{\Delta R_p \sqrt{2\pi}} \exp\left\{-\frac{(x-R_p)^2}{2\pi.\Delta R_p^2}\right\} \qquad 3.12$$

where N (x) is the ion concentration.

3.1.6 Simulation of ions implantation

Before any irradiation or implantation experiments, simulations are performed to predict the optimum experimental parameters Stopping and Range of Ions in Matter (SRIM) developed by Ziegler *et al* [16]. SRIM is a famous program used for the simulation of irradiation or

implantation experiment. SRIM simulation is a computer program that uses Monte Carlo (MC) program to calculate damage distribution, damage range, ion range, and transmitted ions. It treats all targets as amorphous, thereby ignoring the potential contribution of channelling or orientation dependent occurrences to range distributions. Simulations of 360 keV silver (Ag), 280 keV strontium (Sr) and 17 keV helium (He) ions implanted into SiC were performed using SRIM 2013.

It is necessary to select some parameters before running the program such as type of ions, energy, substrate, type of calculations and outputs required. In this study silver, strontium, and helium implantation into SiC were simulated. SRIM predictions are based on the following approximations:

- The crystal structure is not considered.
- The material used is fully amorphous, and the program includes binary collision.
- The electronic stopping power is an averaging fit to a large number of experiments.
- Recombination of knocked off atoms (interstitials) with vacancies, an effect known to be very important in metal heat spikes, is neglected.

SRIM prediction results are discussed together with implantation experimental results in the results and discussion section.

References

1. Eckstein, W. (2013). Computer simulation of ion-solid interactions (Vol. 10). Springer Science & Business Media.
2. Wang, Y., & Nastasi, M. A. (Eds.). (2009). Handbook of modern ion beam materials analysis (pp. 65-92). Warrendale: Materials Research Society.
3. Jain, I. P., & Agarwal, G. (2011). Ion beam induced surface and interface engineering. Surface Science Reports, 66(3-4), 77-172.
4. Thabethe, T. T. (2014). RBS Investigation of the Diffusion of Implanted Xenon in 6H-SIC (thesis for Doctoral, University of Pretoria).
5. Zhang, Y., Aidhy, D. S., Varga, T., Moll, S., Edmondson, P. D., Namavar, F., & Weber, W. J. (2014). The effect of electronic energy loss on irradiation-induced grain growth in nanocrystalline oxides. Physical Chemistry Chemical Physics, 16(17), 8051-8059.
6. Backman, M. (2012). Effects of nuclear and electronic stopping power on ion irradiation of silicon-based compounds.
7. Machaka, R. (2008). Ion Beam Modifications of Boron Nitride by Ion Implantation (thesis for Doctoral, University of the Witwatersrand).
8. Abdelbagia, H.A.A. (2019). Effect of swift heavy ion irradiation and annealing on the microstructure and migration behaviour of implanted Sr and Ag in SiC (thesis for Doctoral, University of Pretoria).
9. Ziegler, J. F. (Ed.). (1988). Ion implantation science and technology. Elsevier.
10. Bethe, H. (1930). Zur theorie des durchgangs schneller korpuskularstrahlen durch materie. Annalen der Physik, 397(3), 325-400.
11. Kamaratos, E. (1984). The mean excitation energy for stopping power I, the Bragg rule, and chemical and phase effects. Application of a statistical treatment to the determination of I for chemically bound particles. Chemical Reviews, 84(6), 561576.
12. Feldman, L. C., & Mayer, J. W. (1986). Fundamentals of surface and thin film analysis. North Holland, Elsevier Science Publishers, P. O. Box 211, 1000 AE Amsterdam, the Netherlands, 1986.

13. Lindhard, J., & Scharff, M. (1953). Energy loss in matter by fast particles of low charge.
14. Fink, D., Biersack, J. P., Chen, J. T., Städele, M., Tjan, K., Behar, M., & Zawislak, F. C. (1985). Distributions of light ions and foil destruction after irradiation of organic polymers. Journal of applied physics, 58(2), 668-676.
15. Chu, W. K. (1976). Calculation of energy straggling for protons and helium ions. Physical Review A, 13(6), 2057.
16. Ziegler, J. F., & Biersack, J. P. (1985). The stopping and range of ions in matter. In Treatise on heavy-ion science (pp. 93-129). Springer, Boston, MA.

Chapter 4

Analytical techniques

This chapter discusses techniques that were used to investigate the influences of He ions in the migration behaviour of Ag and Sr co-implanted into SiC. These techniques are Raman spectroscopy, Rutherford backscattering spectrometry (RBS), and the scanning electron microscopy (SEM), heavy elastic recoil detection analyses (ERDA) and atomic force microscopy (AFM). The experimental details of these techniques are discussed in chapter 5.

4.1 Raman Spectroscopy

Raman spectroscopy is a non-destructive technique that relies on the scattering of light, where molecular scatters incident light from a high-intensity laser light source. The method relies on the collision of light with a chemical bond in the sample. Monochromatic light, such as laser light, interacts with molecules in a way that most of the light is transmitted and a small amount of light is scattered into different direction.

When the sample interacts with incident light, a photon becomes excited to a virtual state from its original energy level, and then returns to its original level of energy. As a result, incident light and scattered light do not transfer energy. During incident and scattering processes, no changes occur in photon frequency or wavelength and this called the elastic scattering or Rayleigh scattering [1]. However, when a photon falls back to a level of energy different from its original level, energy is transferred, the laser photon is shifted up and down, and this allows information about the system's vibration mode to be determined, which is called inelastic scattering. [2]. First prediction of the Raman scattering of light by Smekal was made in 1923 [3]. Raman scattering is named after Chandraseknama Venkata Raman, who discovered inelastic scattering [4].

Examples of inelastic collisions include stoke and anti-stoke Raman scattering. The stoke Raman scattering process begins at the initial energy level. After being excited to a virtual state, it falls back to a higher energy level, which is different from its original energy level. Therefore, the frequency of incident light is higher than that of scattered light [5]. In anti-stoke Raman scattering, photons are excited to a virtual state from their vibrational energy level and drop back down to a lower energy level, thus, incident light has a lower frequency than scattered light. Fig. 4.1 shows the difference in energy between incident and scattered photons by the

arrows of various lengths. Equation 4.1 is used to calculate the Raman shift in wave numbers given in cm^{-1}[6].

$$\tilde{\upsilon} = \frac{1}{\lambda_{incident}} - \frac{1}{\lambda_{scattered}} \qquad 4.1$$

Where λ's are the wavelengths (in cm) of the incident and Raman scattered photons, respectively

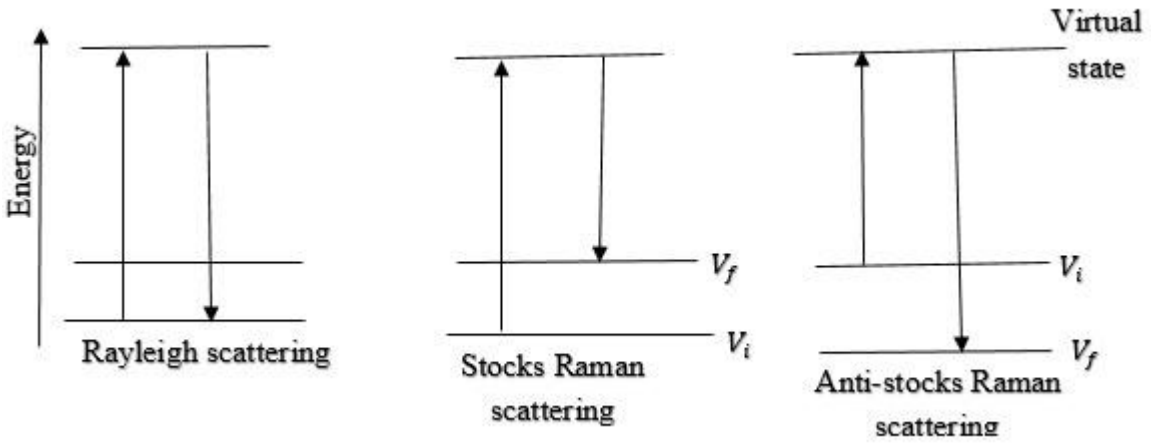

Figure 4. 1: *Energy level diagram representing the state involved in Raman scattering.*

4.1.1 Raman Effect

When the light of a certain wavelength collides with a molecule, most photons are scattered elastically having the same energy as incident photons. However, a small portion is inelastically scattered meaning that the energy of the scattered photon is not the same as the energy of the incident photon. This is known as the Raman Effect.

The energy difference between the incident and the Raman scattered photon is the same as the energy of a vibration quantum of the scattering molecule. A plot of the intensity of scattered light versus energy difference is called a Raman spectrum.

Raman scattering is the result where molecular vibration can change the polarizability. The change is explained by the polarizability derivative, $\frac{d\alpha}{dQ}$,where Q is the normal coordinate of the vibration. The selection rule for a Raman-active vibration, that there be a change in polarizability during the vibration process $\frac{\partial\alpha}{\partial q} \neq 0$.

When a photon collides with a molecule, dipole moment P is induced by the electric field in the molecule as shown in Equation 4.2 [5].

$$P = \alpha E \quad (4.2)$$

The proportionality constant α is the polarizability of the molecule and is a measure of the ease with which the electron cloud around a molecule can be distorted. In the case of the anisotropic molecule, α reduces to a scalar.

The time dependence of the electromagnetic field given by equation 4.3 [6]:

$$E = E_0 \cos(w_q t) \quad (4.3)$$

Where E_0 is the maximum amplitude of the electric field and t is the time.

The incident dipole moment P in equation 4.2 becomes [6]:

$$P = \alpha E_0 \cos(w_q t) \quad (4.4)$$

The molecular polarization normally changes when the bond length changes. The bond length oscillates at the vibrational frequency. Then equation 4.4 becomes [7]:

$$P = [\alpha_0 + (\frac{\partial \alpha}{\partial q})\, q_0\, q_0 \cos(\omega_q t)]_0 \cos(\omega_0 t)$$

$$= \alpha_0 E_0 \cos(\omega_o t) + q_0 E_0 (\frac{\partial \alpha}{\partial q})\, q_0 \cos(\omega_q t)\cos(\omega_o t) \quad (4.5)$$

From the relation: cos n cos m = $\frac{1}{2}[\cos(n+m) + \cos(n-m)]$.

Then equation 4.4 is written as:

$$P = \alpha_0 E_0 \cos(\omega_o t) + \frac{1}{2}(\frac{\partial \alpha}{\partial q})_{q0}\, q_0 E_0 [\cos(\omega_0 + \omega_q) + \cos(\omega_0 - \omega_q)] \quad (4.6)$$

First-term, if the is perfectly elastic scattering that is, the incident frequency is the same as scattered frequency; therefore, there is no change in energy. The process is called Rayleigh scattering. The second term is an inelastic collision**,** the molecule will change energy with the incident photon and the frequency is changed, thus the molecule gains energy. This process is known as anti-stoke scattering. Molecule loses energy by the last term which is known as stoke scattering.

4.2 Rutherford backscattering spectrometry (RBS)

Rutherford backscattering spectrometry (RBS) is a technique mostly used for the analysing thin layers or near surface regions of material. RBS is based on the analysis of the energies of the backscattered particles. During the impact of energetic ions on a target material, some are backscattered with different energies depending on the depth of the back scattering event and the mass of the target atom. Hence, the detections and analyses of the backscattered ions give information about the target [8]. This technique is a non-destructive and is able to give information such as the relative atomic concentration at a unit of area as a function of depth [8]. Helium (He) and hydrogen (H) ions are particles that are normally used in RBS (in this case helium ions (He^+)). This subsection discusses RBS in its five major components: the accelerator (the Van de Graaff accelerator), beam line, analysis chamber, detector and data acquisition.

4.2.1 Van de Graaff generator

Van de Graaff accelerators are electrostatic accelerators that are connected to high voltage and low current. The Van de Graaff generator first belt-charged electrostatic generator was discovered by R. J. Van de Graaff in 1931 [9]. A motor-driven belt is mounted between two rollers (pulleys), an insulating column and a spherical or rounded high-voltage terminal electrode which is mounted on top of the insulating column as shown in Figure 4. 2. The belts are electrically charged by brushes or combs of metallic wires connected to direct current (DC) voltage sources. Voltage controls the amount of electric charge applied to the belt. The positive charges are transported by a belt to the terminal electrode. A second brush or comb of metallic wires is used to carry the charge from the belt to the terminal electrode. Electric charges accumulate on the external surface of the terminal electrode. The resulting terminal voltage is a function of the diameter of the terminal electrode. A radio-frequency ion source inside the accelerator is responsible for producing the He^+ ions, which are then accelerated to the beam line. Fig. 4.2 shows the typical Van de Graaff accelerator.

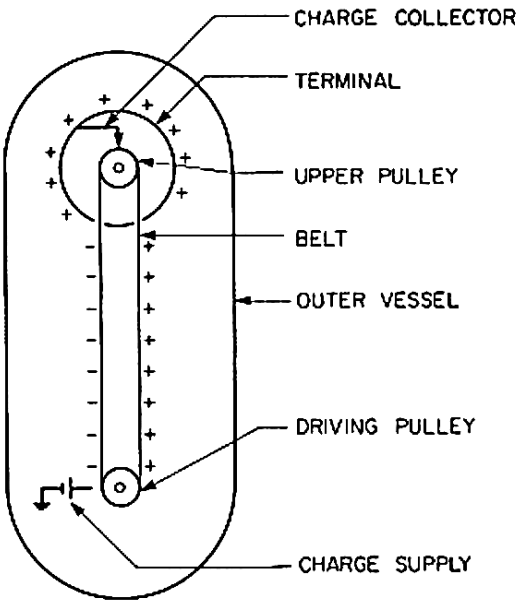

Figure 4. 2: *Schematic diagram of a Van de Graaff accelerator. Taken from [9].*

4.2.2 The beam-line

The beam is accelerated at high energy along a drift tube/beam line that is kept at low pressure before reaching the target. The pressure between 10^{-5} mbar and 10^{-7} mbar is the minimum vacuum necessary to minimise collision probabilities between ions and residual gas molecules. It is necessary for the beam to have a uniform distribution across the cross section of the sample to allow for analysis. Defining cross sections of beams is achieved by collimators.

4.2.3 Analysis chamber

A target is located inside a chamber, where it is exposed to the ion beam. The chamber is also evacuated to lower pressure, in the same manner as the accelerator tube and the beam-line. As part of the air evacuation process, a mechanical pump is used to reduce the chamber pressure to a level of 10^{-2} mbar. This is the starting pressure for the turbo-molecular pump. A turbo pump lowers the pressure to about 10^{-6} mbar. Air is vented from the chamber after analysis to reach atmospheric pressure.

Direct measurements of the beam current are made on the sample. A negative suppression voltage of about 100 volts is applied to the suppressor plates in front of the sample in order to suppress any secondary electrons that might falsify the current measurement. The sample is bombarded by a controlled ion beam at a specific angle (the ion incident angle). A Si detector detects the backscattered ions at a specific backscattered angle with respect to incident beam.

The analogy signal which is a function of backscattered ion's energy is then digitalized by electronics and the spectrum of backscattered energies in channel numbers vs counts are viewed in the computer.

4.2.4 Kinematic factor.

A particle of m_1 moving with an initial velocity v_o and energy E_o interacts with a stationery particle of m_2 as shown in Fig. 4.3, an energy transfer occurs during interaction. After interaction a particle of mass m_1 scatters with velocity v_1 and E_1while a particle with m_2 recoils with, velocity v_2, and energy E_2. Using the conservation of energy and momentum principles, it is possible to solve the elastic collision between two masses m_1 and m_2. [8], the ratio of the projectile energy after elastic collision to that before the collision known as kinematic factor (K) can be determined [10]:

$$K = \frac{E_1}{E_0} \tag{4.7}$$

$$K = \frac{E_1}{E_0} = \left[\frac{\sqrt{m_2^2 - m_1 \sin^2\theta} + m_1 \cos\theta}{m_1 + m_2}\right]^2 \tag{4.8}$$

where m_1 and m_2 are the atomic masses of the alpha particle and target atom respectively. E_1 and E_0 are the energies of the incident and backscattered particle and θ is the backscattered angle as shown in Fig. 4.1.

After backscattering, energy only depends on the mass m_1 of the projectile, the mass m_2 of the target atom, and the angle of scatteringθ. If m_1, E_0 and θ are known, then m_2 can be found then, the target element is known. In our RBS experiment, the backscattering angle was 165^o.

The experimental details are presented and discussed in chapter 5.

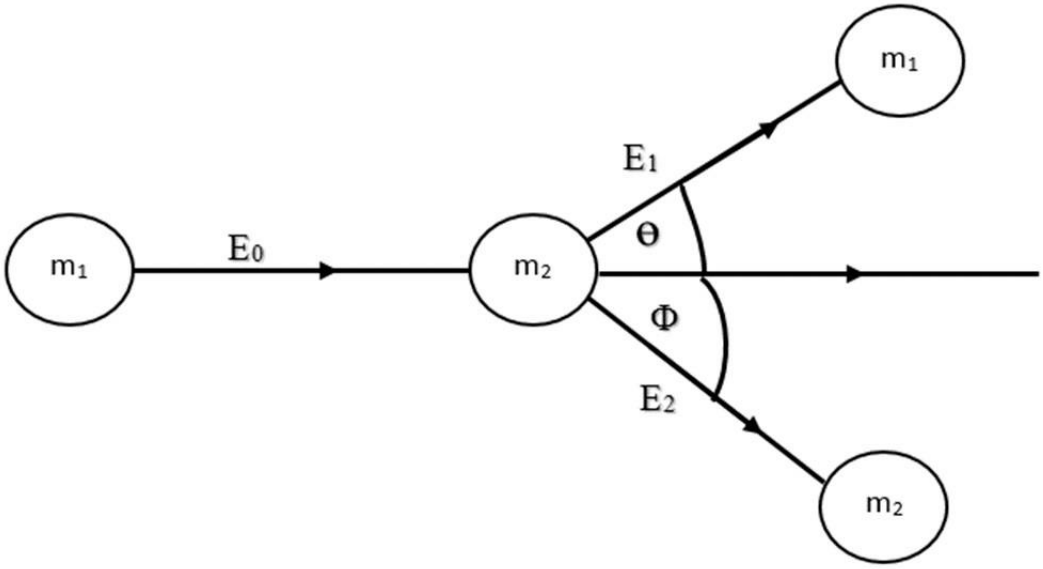

Figure 4. 3: *Diagram illustrating elastic scattering with m_1 and m_2 representing the masses of the incident ions and the recoiling atoms.*

4.2.5 Differential cross section

Differential cross section $^{d\sigma}/_{d\Omega}$ is the probability of a backscattering event to occur. In the laboratory system, Rutherford cross-sections for backscattering are as follows [5]:

$$d\sigma \,/\, d\Omega = \left(\frac{Z_1 Z_2 e^2}{4E}\right)^2 \frac{4\left[\left(m_2^2 - m_1^2 \sin^2\theta\right)^{\frac{1}{2}} + m_2 \cos^2\theta\right]^2}{m_2 \sin^4\theta \left(m_2^2 - m_1^2 \sin^2\theta\right)^{\frac{1}{2}}} \qquad 4.9$$

where θ is the backscattering angle, Z_1 is the atomic of a projectile with mass m_1, Z_2 is the atomic number of target element with mass m_2, e is the electron charge, E is the initial energy of the projectile. From this equation it is quite clear that RBS is more sensitive to heavy element i.e. high Z element and more yields are obtained using low energy ions. The total number of detected particles is given by [11]:

$$B = \Omega \sigma Q\, N \qquad 4.10$$

where σ is deferential cross section, N is the total number of atoms per unit area, Ω is the solid angle detector, Q is the total number for incident particles.

4.2.6 Depth profiling

An incident particle with energy E_o backscatters at the surface with energy KE_o, where K is the kinematic factor, while an incident particle that penetrate the sample loses some energy and has energy E before backscattering at depth *x*. The particle has energy *KE* after backscattering at depth *x*. The particle backscattered at depth *x* loses energy on its way out and emerges out of the surface with energy E_1 as shown in Fig. 4.4 [9, 10].

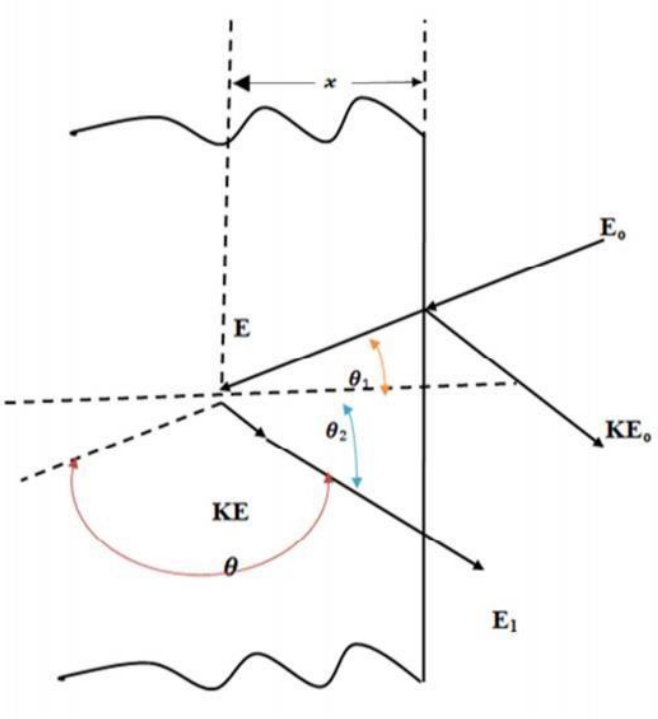

Figure 4. 4: *Schematic illustrating the backscattering event for a particle at a depth of x. Taken from [10].*

As mentioned earlier, an impinging particle loses energy in its inward and outward paths. From Fig. 4.4, the inward path of $x/\cos\theta_1$ and the outward path of $x/\cos\theta_2$ are obtained. The energy loss in an inward path is E_o-E and energy loss in an outward path is KE-E_1 while the particle backscatters on the surface has an energy of KE_o. Assuming a constant energy loss of dE/dx along the inward and outward paths, E and E can be written as:

$$E = E_O - \frac{x}{\cos\theta_1}\frac{dE}{dx} \text{ in} \qquad 4.11$$

and

$$E_1 = KE - \frac{x}{\cos\theta_2}\frac{dE}{dx}\text{ out} \quad (4.12)$$

Eliminating E in equation 4.11 and 4.12, yields to [10]:

$$KE_0 - E_1 = \left[\frac{K}{\cos\theta_1}\frac{dE}{dx}\right] in + \frac{1}{\cos\theta_2}\frac{dE}{dx}\text{ out} \quad (4.13)$$

Taking ΔE as the energy difference between *E* and *KE*:

$$\Delta E = KE_0 - E_1 \quad (4.14)$$

Equation 4.13 can be written as follows:

$$\Delta E = [S] \quad (4.15)$$

where [S] is given by:

$$[S] = \left[\frac{K}{\cos\theta_1}\frac{dE}{dx}\right] in + \frac{1}{\cos\theta_2}\frac{dE}{dx}\text{ out} \quad (4.16)$$

[S] is called the energy loss factor. Using equation 4.18, it is possible to convert the measured energy spectrum into depth.

4.3 Scanning electron microscopy (SEM)

A scanning electron microscope (SEM) is a type of electron microscope that produces images of a sample by scanning the surface with a focused beam of electrons [12]. The incident electrons collide with the atoms in the sample and produce various signals [13]. These signals carry information about the sample's morphology, chemical composition and crystalline structure, and the orientation of material [13]. SEM consists of an electron optical column mounted on a vacuum chamber as shown in Fig. 4.5.

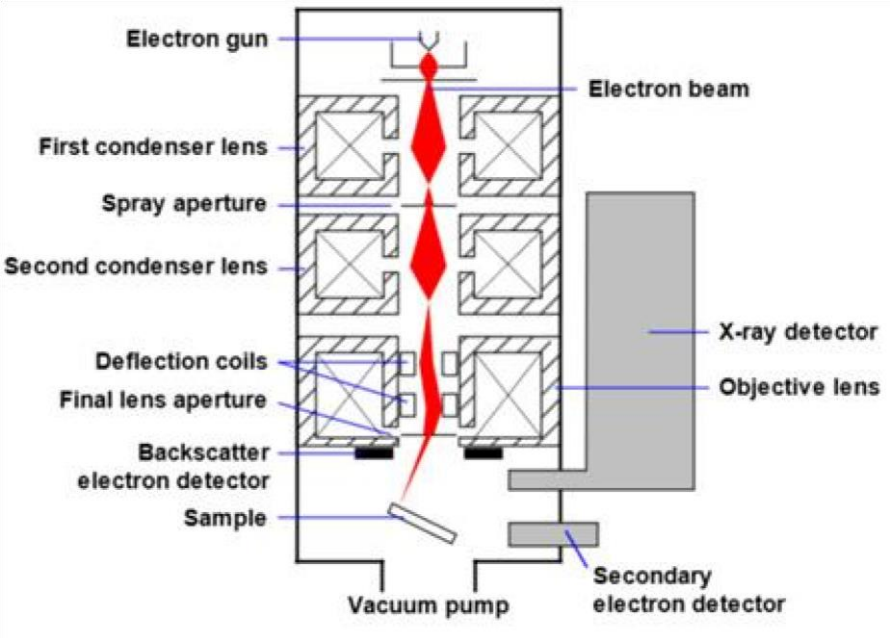

Figure 4. 5: *Schematic representation of scanning electron microscopy. Taken from [14].*

4.3.1 Electron Column

The electron beam is generated by an electron gun mounted on top of the column. There are three types of electron beam, which are field emission gun, tungsten filament, and lanthanum hexaboride. A field emission gun is the most commonly used. Due to the electrons being emitted from smaller areas than FEG sources, this particular emission source is on the order of nanometers, which is in comparison to microns for other emission sources. [15]. In the SEM, a high vacuum is necessary, in order to maintain a stable electron gun, 10^{-4} Pa (~ 10^{-6} torr) must be maintained. [16]. Electrons move freely in vacuum, which results in a high resolution image, i.e., without a vacuum, electrons collide with air molecules, causing the beam to become less intense and unstable. Similarly, other gas molecules, which could come from the sample or the microscope itself, could form compounds and condense on the sample [13].

Generally, electrons are primary accelerated by the positive charge of an anode that is adjustable from 200 V to 30 kV. After the electron beam passes the anode, it is focused by a system of condenser lenses and apertures before being directed towards the surface. There are objective lenses located below condenser lenses and closest to the sample. The apertures are placed between the condenser lenses and the objective lenses. Placing these lenses below the electron gun allows adjustment of the electron beam diameter, as accurate beam is required for SEM. Therefore, the electron beam is mainly focused down to 1000 times its original size when it passes through the electron trap.

4.3.2 Electron Beam-Specimen Interactions

When electrons are accelerated onto a material, several collisions occur with the atoms of the target sample. Electrons directed at the sample will scatter in different directions. These are divided into an elastic or inelastic scattering of the electron. Elastic scattering occurs when there is no energy loss for the incident electron, and vice versa in the case of inelastic scattering. As mentioned earlier, the interaction between an electron beam and a sample produces a large number of signals. The emitted signals are secondary electrons (SE), backscattering electrons (BSE), Auger electrons and x-rays (see Fig. 4.6), which are detected by the detector and used to form an image on the computer [16]. Fig. 4.7 shows the depths at which the various signals are emitted.

The production of backscattered electrons varies based on the weight of the element. An element with bigger nuclei can scatter incident electrons more strongly than a lighter element. The latter appears darker in the SEM image. The SE is the result of inelastic scattering between the electron beam and the atoms of the sample. SE has a low energy of approximately 50 eV and can be absorbed easily [17]. They are emitted from the surface of the sample when energy is transferred from the electron to the spacemen' electron. The BSE are electron that are reflected from the atomic surface and have much higher energy than the SE, because they come from much deeper within the target atoms. BSE are due to elastic scattering when the electron beam interacts with nuclei of the sample. They scatter from the sample with little energy loss and are able to travel greater depths within the sample [18].

X-rays are emitted when an electron fills an inner-shell vacancy of an atom. These vacancies are created by the emission of secondary electrons. Auger electrons are electrons that are emitted from the near surface of the sample because of their low kinetic energies. Auger electron are also emitted when electrons from the high energy level falls into a vacancy in a shell created during the SE emission.

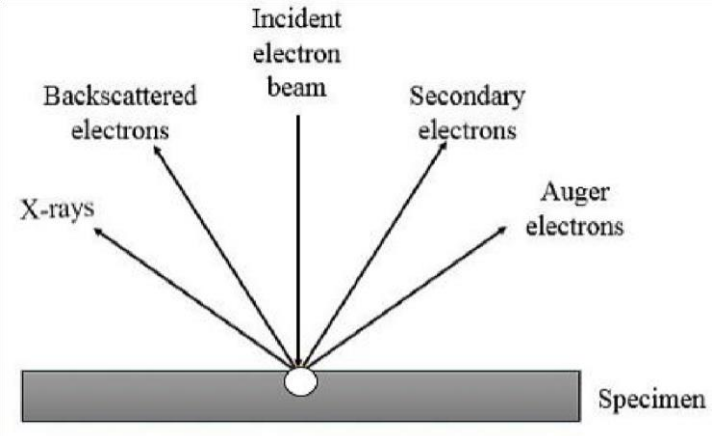

Figure 4. 6: *A schematic diagram illustrating the signals which are emitted when an electron beam interacts with the sample.*

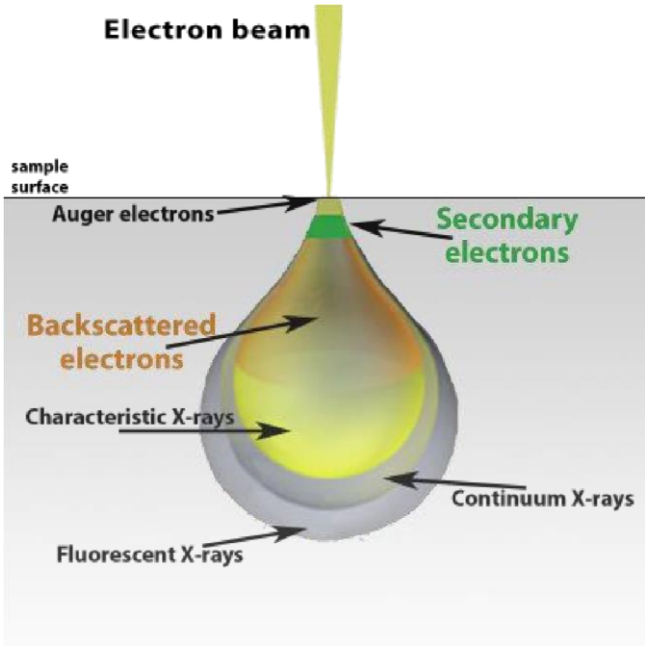

Figure 4. 7: *A schematic diagram illustrating the signals generated by the electron beam sample interaction at different depths. Taken from [9].*

4.4 Atomic force microscopy (AFM)

AFM is a type of microscope that was developed in 1985 to measure local properties such as surface topography using probes [19]. The AFM technique is used to study the characteristics of phases, grains, and surfaces of many materials, including metallic, ceramic, organic, and inorganic [20]. Various imaging modes are now available, providing information about the sample surface. Additionally, AFM offers three-demotion topographies and two types of imaging modes: contact and dynamic (tapping or noncontact) modes [21]. AFM cantilever or tip is in constant contact with the material surface during contact mode and a cantilever works under repulsive force since when it moves closer to the surface, the repulsive force increases [22]. The cantilever is constantly in contact with the material when in a contact mode, so damage to the material is possible. While the tip or cantilever is vibrating close to the surface of the material during non-contact, the material is not damaged.

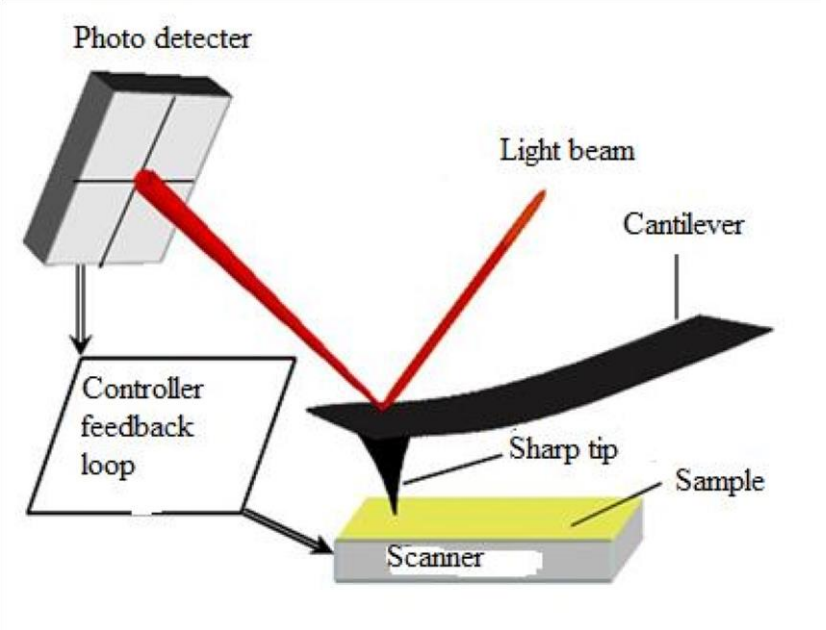

Figure 4. 8: *Diagram showing atomic force microscopy. Taken from [23].*

4.4.1 Principle of atomic force microscopy (AFM)

Fig. 4.8 illustrates the AFM components. An AFM is fitted with a sharp tip at one end of the cantilever. The cantilever tip is made up of DDSEP-FM-V2. With the assistance of double-sided tape, the samples were mounted on aluminium stubby. AFM data is obtained by sensing the surface of the sample using a cantilever [24]. An AFM scans a sample surface by using a cantilever and measures the force between the surface and the cantilever [25]. Force of attraction causes the cantilever to bend towards the surface as it moves toward the sample. Although

repulsive force increases as the cantilever moves near the surface, the cantilever will disengage from it due to increasing repulsive force. This causes the material to move up and down as a result of the laser beam directed at the back of the cantilever. Photodiodes are used to detect reflected laser beams. Reflected lasers can be used for a variety of data sorts.

4.5 Heavy-ion time-of-flight elastic recoil detection (HI-TOF-ERD) analysis

HI-TOF-ERDA is an elastic recoil detection analysis that used heavy energetic ions to get information about the elemental analysis and their depth profiles in materials. ERDA like RBS depends on the kinematic factor, differential scattering cross-section and the stopping powers. The advantage of this technique over RBS is its ability to detect lighter elements. In this study, ERDA was used to monitor the depth profiles of the implanted He, Ag and Sr into SiC before and after annealing at 1000 ^{o}C.

In a simple HI-TOF-ERD set-up shown in Fig. 4.9, an energetic heavy-ion impinges a target surface at a grazing incident angle, α, at a shallow depth and a subsequent recoil atom is forward recoil scattered at a recoil angle ϕ.

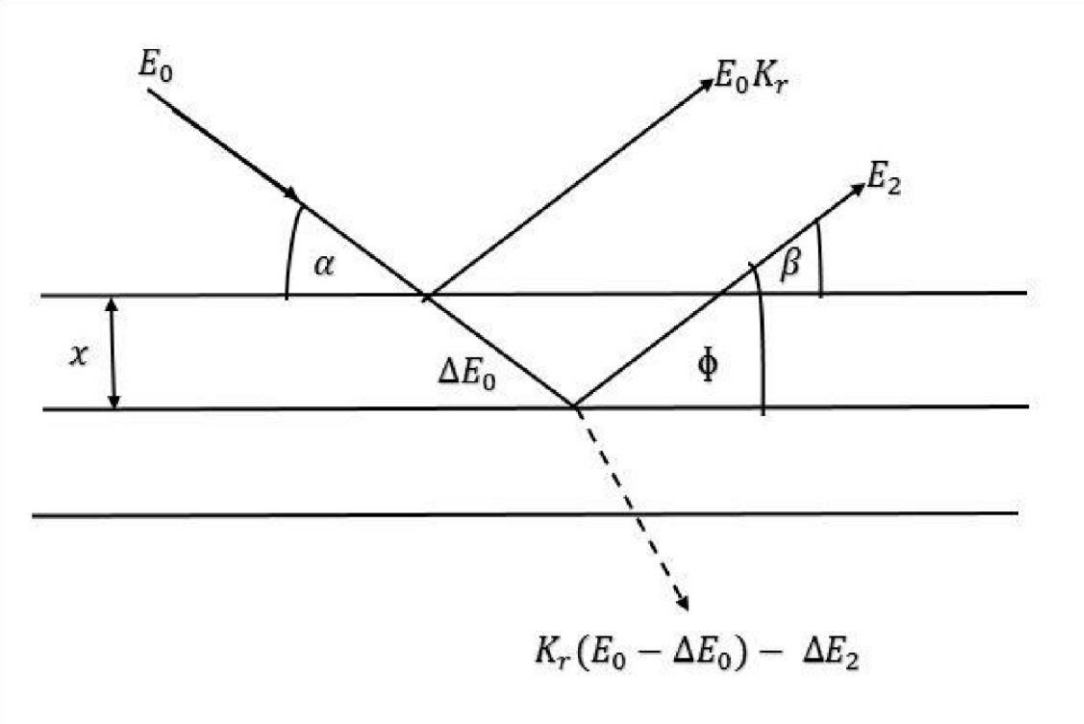

Figure 4. 9: *Principle of ERDA. Φ, α, and β are recoil angle, incident angle, and exit angle, respectively, x is the depth where the incident ion collides with the target atom.*

If conservation of momentum and energy are used to calculate the energy transfer from the projectile heavy-ion of mass m_1 to the recoiling target atom of mass m_2, the ratio of the recoil energy E_2 to the incident ion E_0 in the laboratory frame can be determined [26]:

$$\frac{E_2}{E_0} = K_r = \frac{4m_1m_2}{(m_1+m_2)^2}\cos^2\varphi \qquad 4.17$$

where K_r is the recoil kinematic factor, E_2 and E_0 are recoil and incident energies. If the collision take place inside the sample, the incident ions and recoil atoms lose their kinetic energy as they travel within the sample. Therefore, the kinetic energy of the recoil atom at the surface becomes less than that of incident energy. For example, in Fig. 4.9, When the incident ion collides with the target atom at the depth x perpendicular to the surface, the kinetic energy of the recoil atom at the sample surface, $E_2(x)$, is expressed as follows [27]:

$$E_2(x) = K_r\,(E_0 - \Delta E_0) - \Delta E_2 \qquad 4.18$$

where ΔE_0 and ΔE_2 indicate the energy losses of incident and recoil ions in the sample. Equation 4.2 can be expressed using the stopping power as follows [28]:

$$E_2(x) = K_r\left[E_0 - \int_0^{x/\sin\beta} S_p(x)dx\right] - \int_0^{x/\sin(\phi-\beta)} S_r(x)dx \qquad 4.19$$

where Sp, Sr and β are the stopping powers of the projectile ions and recoil atoms. The term in parenthesis indicates the projectile residual energy just before the collision, while the second term gives the energy loss of the recoils as they emerge out of the sample.

The stopping power of matter for ion beams is the key quantity to converting energy into depth information because by definition [28]:

$$\lim_{\Delta x\to 0}\frac{\Delta E}{\Delta x} = \frac{\delta E}{\delta x} = s \qquad 4.20$$

where δE is the ion energy loss and δx is the distance traversed. This equation also relates the minimum analysable depth, the depth resolution Δx, to the minimum discernible energy, the energy resolution ΔE.

References

1. Das, R. S., & Agrawal, Y. K. (2011). Raman spectroscopy: recent advancements, techniques and applications. Vibrational spectroscopy, 57(2), 163-176.
2. Xu, Z., He, Z., Song, Y., Fu, X., Rommel, M., Luo, X., & Fang, F. (2018). Topic review: Application of Raman spectroscopy characterization in micro/nanomachining. Micromachines, 9(7), 361.
3. Smekal, A. Zur quantentheorie der dispersion. Naturwissenschaften. 1923, 11, 873–875
4. Raman, C. V., & Krishnan, K. S. (1928). A new type of secondary radiation. Nature, 121(3048), 501-502.
5. Xu, Z., He, Z., Song, Y., Fu, X., Rommel, M., Luo, X., & Fang, F. (2018). Topic review: Application of Raman spectroscopy characterization in micro/nanomachining. Micromachines, 9(7), 361.
6. Olego, D., & Cardona, M. (1982). Pressure dependence of Raman phonons of Ge and 3C-SiC. Physical Review B, 25(2), 1151.
7. Ferraris, S., & Padoan, G. (2018). Preparation and characterization of Ti-6Al-4V surfaces functionalized with silver for antibacterial purposes: study of ionic and nanoparticles release mechanism., Han, B., Wang, Z., Devi, N., Kondamareddy, K. K., Wang, Z., Li, N., & Liu, C. (2017). RBS depth profiling analysis of (Ti, Al) N/MoN and CrN/MoN multilayers. Nanoscale Research Letters, 12(1), 1-8.
8. Mayer, J. W., Nicolet, M. A., & Chu, W. K. (1978). Backscattering Analysis with MeV 4 He Ions. Material Characterization Using Ion Beams, 333-366.
9. Bubert, H., Rivière, J. C., Arlinghaus, H. F., Hutter, H., Jenett, H., Bauer, P., & Friedbacher, G. (2000). Surface and Thin Film Analysis. Ullmann's Encyclopedia of Industrial Chemistry.
10. Kanana, M. (1980). Scanning Electron Microscopy: Principle, Components and Applications M.T. Postek, K.S. Howard, A.H. Johnson and K.L. McMichael, Scanning Electron Microscopy, A Student's Handbook,
11. Watt, I. M. (1997). The principles and practice of electron microscopy. Cambridge University Press.

12. Brandon C Introduction to Scanning Electron Microscopy, [online] Available at: http://cfamm.ucr.edu/documents/sem-intro.pdf [Accessed 26 Apr. 2017].

13. Mtshonisi, N. (2020). Effects of Ag and Sr dual ions implanted into SiC (MSc dissertation, University of Pretoria).

14. Zhou, W., Apkarian, R., Wang, Z. L., & Joy, D. (2006). Fundamentals of scanning electron microscopy (SEM). In scanning microscopy for nanotechnology (pp. 1-40). Springer, New York, NY.

15. Serman, N. (2011). Production of X-rays and Interactions of X-rays with Matter. Columbia University in the City of New York.

16. Shinato, K. W., Huang, F., & Jin, Y. (2020). Principle and application of atomic force microscopy (AFM) for nanoscale investigation of metal corrosion. Corrosion Reviews, 38(5), 423-432.

17. Johnson, D., & Hilal, N. (2015). Characterisation and quantification of membrane surface properties using atomic force microscopy: A comprehensive review. Desalination, 356, 149-164

18. Rourk, C. J. (2019). Conductive atomic force microscopy data from substantia nigra tissue. Data in brief, 27, 103986.

19. Pletikapić, G., & Ivošević DeNardis, N. (2017). Application of surface analytical methods for hazardous situation in the Adriatic Sea: monitoring of organic matter dynamics and oil pollution. Natural Hazards and Earth System Sciences, 17(1), 31-44.

20. Belec, L., & Joliff, Y. (2016). Mechanically affected zone in AFM force measurements—Focus on actual probe tip geometry. Materials & Design, 104, 217226.

21. Heim, T., Lmimouni, K., & Vuillaume, D. (2004). Ambipolar charge injection and transport in a single pentacene monolayer island. Nano Letters, 4(11), 2145-2150.

22. Yasuda, K., Kajitori, Y., Oishi, M., Nakamura, H., Haruyama, Y., Saito, M., & Hibi, S. (2019). Upgrades of a time-of-flight elastic recoil detection analysis measurement system for thin film analysis. Nuclear Instruments and Methods in Physics Research Section B: Beam Interactions with Materials and Atoms, 442, 53-58.

23. Shinato, K. W., Huang, F., & Jin, Y. (2020). Principle and application of atomic force microscopy (AFM) for nanoscale investigation of metal corrosion. Corrosion Reviews, 38(5), 423-432.

24. Adams, F., & Barbante, C. (2015). Particle-based imaging techniques. In Comprehensive Analytical Chemistry (Vol. 69, pp. 315-337).
25. Brijs, B., Sajavaara, T., Giangrandi, S., Arstila, K., Vantomme, A., & Vandervorst, W. (2005). Characterization of high and low k dielectrica using low-energy Time of Flight Elastic Recoil Detection. Microelectronic engineering, 80, 106-109.
26. Bergmaier, A., Dollinger, G., Frey, C. M., & Faestermann, T. (1995). Quantitative elastic recoil detection (ERD). Fresenius' journal of analytical chemistry, 353(5), 582584.
27. Wang, Y., & Nastasi, M. A. (Eds.). (2009). Handbook of modern ion beam materials analysis (pp. 65-92). Warrendale: Materials Research Society.
28. Ross, G. G., Terreault, B., Gobeil, G., Abel, G., Boucher, C., & Veilleux, G. (1984). Inexpensive, quantitative hydrogen depth-profiling for surface probes. Journal of Nuclear Materials, 128, 730-733.

Chapter 5

Experimental procedures

In this study, polycrystalline SiC wafers from Valley Design Corporation were used. $^{109}Ag^{+}$ and $^{87}Sr^{+}$ were sequentially implanted into polycrystalline SiC at 600 °C respectively. Some of the co-implanted samples were then implanted with He ions at a temperature of 350 ^{o}C. The morphological and structural evolutions were monitored by scanning electron microscopy (SEM) and Raman spectroscopy respectively. The changes in the surface topography were monitored by atomic force microscopy (AFM) and the migration of implanted Ag&Sr was monitored by Rutherford backscattering spectrometry (RBS). Fig. 5.1 shows a schematic diagram of the experimental procedure.

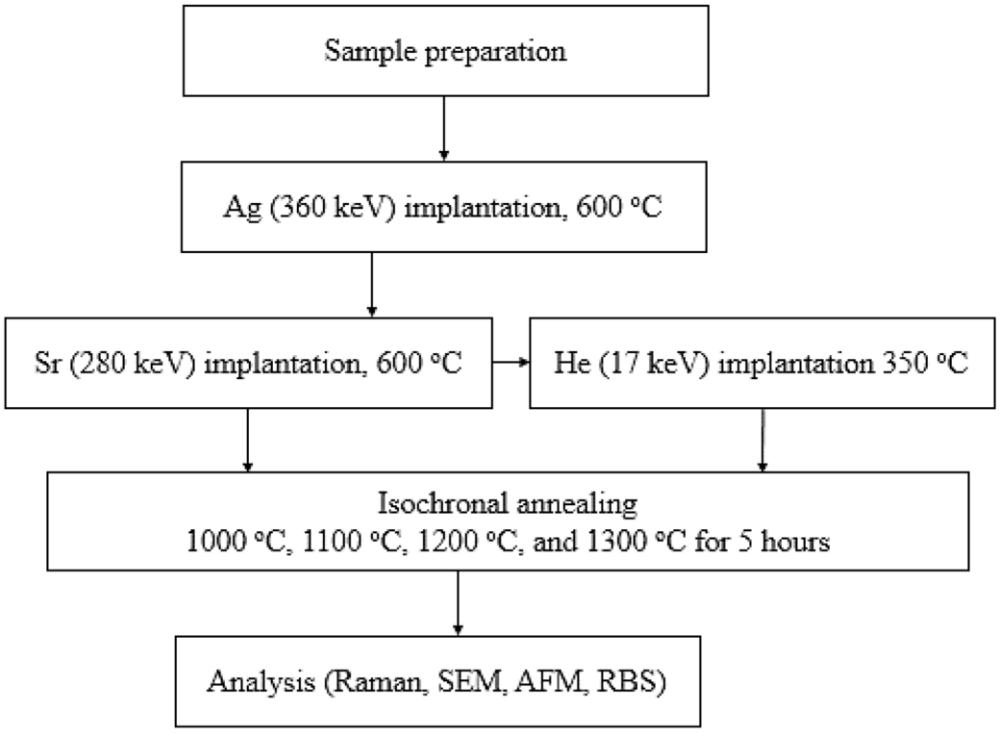

Figure 5. 1: *Schematic diagram of the experimental procedure.*

5.1 Sample preparation

Before SiC wafers were implanted, they were cleaned in an ultrasonic bath with acetone and methanol for 10 minutes to remove any contamination, followed by rinsing them with de-ionized water for approximately 3 minutes. The cleaning process was repeated about four to five times. Finally, they were put in an oven (blow dry) for10 minutes.

5.2 Implantation

Polycrystalline silicon carbide (SiC) was used as a substrate in this study. The implantation of Ag and Sr was done at Institut für Festkörperphysik, Friedrich-Schiller-Universität, Jena, Germany. Silver (Ag) ions of 360 keV were first implanted to a fluence of $2\times10^{16}cm^{-2}$ at a temperature of 600 ^{o}C. On the same samples, strontium (Sr) ions of 280 keV were implanted to a fluence of $2\times10^{16}cm^{-2}$ at a temperature of 600 ^{o}C. Some of the co-implanted samples were then implanted with helium (He) ions of 17 keV to a fluence of $1\times10^{17}cm^{-2}$ at a temperature of 350 ^{o}C. Helium implantation was performed at iThemba LABS, Gauteng, South Africa.

5.3 Annealing

A computer-controlled Webb 77 graphite furnace was used for annealing samples at a temperature ranging from 1000 ^{o}C to 1300 ^{o}C for 5 hours in steps of 100 ^{o}C under vacuum in the order of 10^{-5} mbar. Crucible was to put samples inside to prevent them from contamination. The oven was evacuated at a pressure of about 10^{-5} to 10^{-7} mbar before starting the annealing process. The oven was cleaned by heating it at a temperature of 200 ^{o}C for 1 hour. This was done to make sure that pressure is always at 10^{-5} mbar during annealing. The temperature is controlled by a Eurotherm 2704. This controller is connected to a thermocouple and pyrometer that are used to measure the temperature. Thermocouple is used to measure temperature less than 1475 ^{o}C and pyrometer measures temperature greater than 1525 ^{o}C. The heating element heat up to the required temperature and time duration.

Once the annealing process was done, the oven was switched off and let to cool down to room temperature naturally. Once the oven was at RT, the vacuum pump was switching off, then argon gas was used to bring the pressure to atmospheric pressure. Then sample was taken out of the oven. Fig. 5.2 shows a typical temperature-time graph of the sample annealed at 1000 ^{o}C.

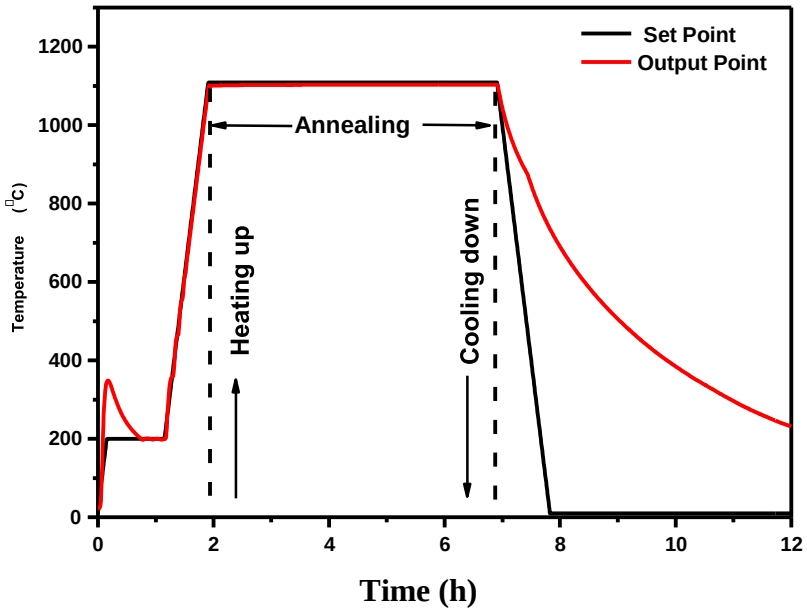

Figure 5. 2: *A typical e temperature (°C)-time (h) graph of sample annealed at 1000 °C for 5 hours.*

5.4 Measurement conditions

5.4.1 Raman spectroscopy

The structural changes of the implanted sample before and after annealing were investigated using Raman spectroscopy technique (WITec alpha 300 R, Germany). To analyses the vibrational modes of the sample, laser wavelength of 532 nm and laser power of 20 nm with integration time of 10 s were collected using a 100 × objective lens. Area of interest was measured using Quantachrome (NOVAtouch NT 2L×-1, Volts 220, USA) deriving by Quantachrome TourchWin Software Version: 1.22

5.4.2 Scanning electron microscopy (SEM)

The morphological changes of samples (Ag&Sr-SiC) before and after annealing was analysed using a field emission gun (FEG-SEM) at the University of Pretoria with a Ziess Ultra 55 using in-lens detector. During SEM measurements 2 kV was used as accelerating voltage, and the spatial resolution used was 200 nm.

5.4.3 Atomic force microscope (AFM)

Morphology of the sample (Ag&Sr&He-SiC) were investigated using AFM from the University of Pretoria. In this study, contact (tapping) mode AFM was used. Samples were mounted with aluminium stubby using double sided tape with cantilever of tip DDSEP-FMV2. Samples were

analysed using Veeco dimension icon with scanAsyst. AFM images was obtained with a scan size of 20μm × 20μm. Nanoscope analysis was used to obtain AFM images.

5.4.3 Rutherford backscattering spectrometry (RBS)

RBS analysis was performed at iThemba LABS, Cape Town South Africa on the as-implanted Ag&Sr&He-SiC sample and Ag&Sr&He-SiC annealed at 1100 ºC for 5 hours. A 6 MV Pelletron Tandem Accelerators that was used for RBS measurements. The backscattered He^{+} ions (backscattered from the samples) were detected using a solid-state detector with a solid angle of 0.0460 msr was placed in IBM geometry with the sample. The charge collected per spectrum was 0.500 μC. OMDAQ software version 3 [3.100] supplied by Oxford Microbeams was used to acquire the RBS data.

5.4.4 Elastic Recoil Detector Analysis (ERDA)

Elastic Recoil Detection Analysis (ERDA) was used to monitor the presence of all implanted ions. ERDA's advantage lies in its ability of detecting He ions. To analyse the contributions of each ion, ERDA employed a Time of Flight (ToF) detector system using a 30 MeV Au^{7+} ion beam. A silicon PIPS® detector is used to measure the recoil ions' energy simultaneously with their time of flight, using two carbon foil-based timing detectors spaced 0.60 m apart. As a result of coincidence measurements, recoil particles are separated by atomic mass. In order to determine elemental energy spectra, 2D plots of ToF versus Energy can be generated, then utilize an energy-depth conversion algorithm to calculate depth profiles.

Chapter 6

Results and discussion

In this study, the effect of helium (He), strontium (Sr) and silver (Ag) implanted into silicon carbide (SiC) on the structural changes and migration of the implants was investigated. Ag ions of 360 keV were implanted into polycrystalline SiC to a fluence of 2×10^{16} cm^{-2} at 600 ^{o}C. On the same sample, Sr ions of 280 keV were also implanted to a fluence of 2×10^{16} cm^{-2} at 600 ^{o}C. Some of the co-implanted samples were then implanted with 17 keV He ions to a fluence of 1×1017 cm^{-2} at 350 ^{o}C. The samples were then annealed at temperatures ranging from 1000 ^{o}C to 1300 ^{o}C in steps of 100 ^{o}C for 5 hours. The as-implanted and annealed were characterized by Raman spectroscopy, Scanning Electron Microscopy (SEM), Atomic force microscopy (AFM), Elastic recoil detection analysis (ERDA) and Rutherford backscattering spectroscopy (RBS). This chapter presents and discusses the findings.

6.1 Ag and Sr implants

6.1.1 Simulation results

Fig. 6.1 shows the simulated depth profiles and displacement per atom (dpa) from SRIM 2013 [1] for 360 keV Ag and 280 keV Sr ions implanted into SiC. A density of 3.21g/cm^3 and displacement energies of 35 and 20 eV for silicon and carbon atoms, respectively, were used in the simulations [2]. The detailed calculations in full cascade mode was used in the simulations. The ion fluence was converted into displacement per atom (dpa) using equation 6.1 [3]:

$$dpa = \frac{v_{ac}/ion(cm)\times10^{8}\times\varphi(ions.cm^{-2})}{\rho_c(ions.cm^{-2})} \qquad 6.1$$

where v_{ac}/ion(Å) is the vacancy per ion from SRIM 2013, φ is is the ion fluence, ρ_c is the theoretical density of silicon carbide (9.641×10^{22} atom.cm^{-3}). If one assumes that the critical amorphization of SiC is 0.3 dpa [4], both implantations will completely amorphized SiC. However, the implantations were performed at 600 ^{o}C, which is greater than the critical amorphization temperature of SiC (350 ^{o}C) [5]. Therefore, the samples are not expected to be full amorphized under the implantation conditions used in this study. Ag and Sr depth profiles overlap with a projected range around 120 nm below the surface. As shown in Figures 6.1, implantation resulted in a maximum dpa of 60 dpa and 45 dpa for Ag and Sr ions, respectively,

at a depth of 90 nm below the surface. The total dpa of the two ions has a maximum dpa of 106 dpa at a depth of 85 nm.

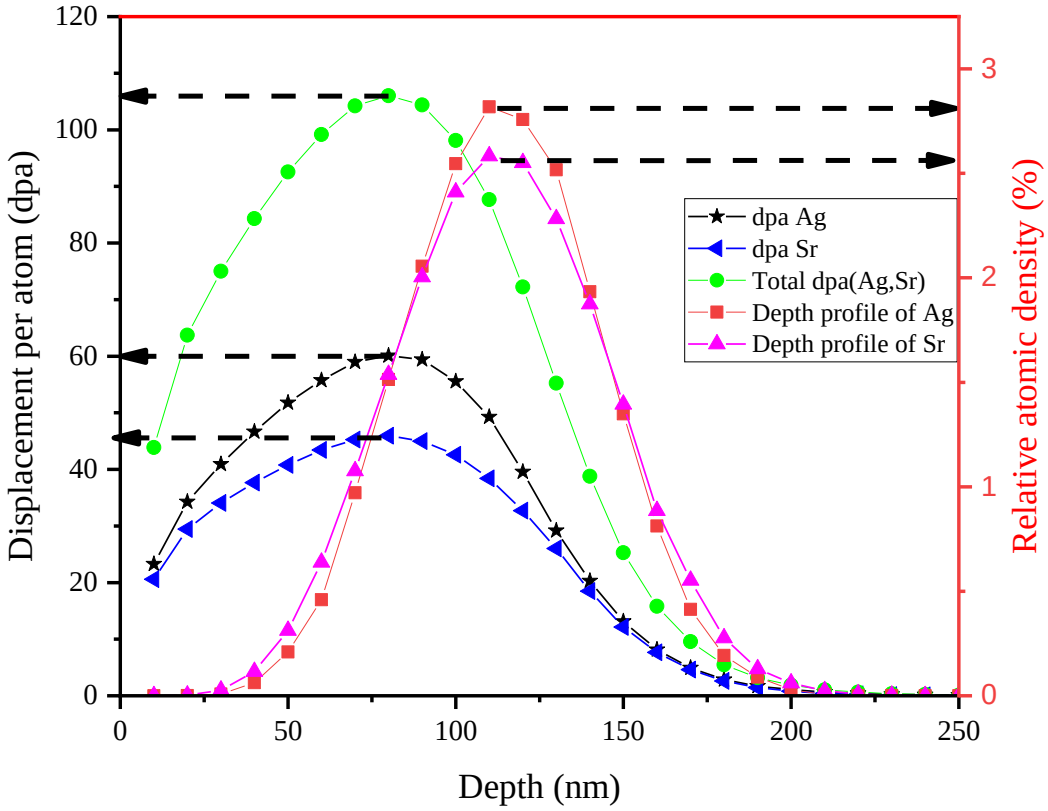

Figure 6. 1: *SRIM 2013 simulated Ag (360 keV) & Sr (280keV) depth profiles and displacement per atom (dpa).*

6.1.2 Raman results

Fig. 6.2 shows the Raman spectra of a virgin SiC and co-implanted sample before and after isochronally annealing at temperatures ranging from 1000 ºC to 1300 ºC for 5 hours in steps of 100 ºC. The Raman spectrum of SiC-Virgin exhibits Raman characteristics peaks intensity of SiC [6]. The Raman spectrum of a virgin sample has a transverse mode (TO) that splits into two peaks around 765 cm^{-1} and 794.3 cm^{-1}, the longitudinal mode (LO) peak around 971.6 cm^{-1} belonging to 3C-SiC and 6H-SiC and two TO overtones peaks at 1516 cm^{-1} and

1715 cm^{-1}. These observations are similar to those reported by [7]. In addition, this Raman spectrum confirms that polycrystalline SiC is mostly composed of 3C-SiC with some 6H-SiC present [7]. The Raman spectrum parameters, i.e., intensity, FWHM and peak shift are highly sensitive to the crystal structure. In particular, defects can reduce the area of the undisturbed region, leading to changes in lattice constants and phonon confinements [8]. From Fig. 6.2, it can be seen that, co-implantation caused the reduction in intensity of Raman peaks accompanied by broadening indicating accumulation of defects without amorphizing the SiC structure as seen in (Fig. 6.2 (b)). The lack of amorphization is due to the implantation temperature (600 ^{o}C) that is greater than the critical temperature of amorphization (350 ^{o}C) [9]. The reduction in intensity is due to a decrease in the number of scattering molecules irradiated by the incident laser caused by high concentration of defects/damage in the implanted SiC [10]. As a result of the annealing at 1000 ^{o}C, the LO mode intensity increased slightly as shown in Fig.6.2 (c). This indicates that some defects have been annealed out. This annealing of defects progress with annealing temperature as seen in (Fig. (d), (e), and (f)), with some still remaining as can be seen from the reduced intensity of Raman spectrum of the sample annealed at 1300 ^{o}C compared to the pristine one.

The changes in full width at half maximum (FWHM), as well as LO peak positions as a function of annealing temperature are shown in Fig. 6.3. Co-implantation resulted in the broadening of FWHM (15.8 cm^{-1}) as compared to FWHM of a virgin sample (11.4 cm^{-1}) further indicating accumulation of defects and poor crystallinity [10]. After annealing at 1000 °C, the FWHM narrowed by 2.7 cm^{-1}, indicating less defects compared to the as-implanted sample. Further annealing resulted in a gradual decrease in FWHM i.e. the crystallinity of silicon carbide increased with increasing annealing temperature. At the highest temperature viz. 1300 °C, the FWHM was about 11.9 cm^{-1}, which is broader than that of a virgin, indicating that defects are still present in the implanted SiC samples [11]. Fig. 6.3 also shows that there was no noticeable variation in the LO mode position after implantation and during annealing up to 1300 °C. This suggests that the interatomic spaces for most of the atoms remained unchanged. There are no new phases formed/observed during the annealing between SiC and Ag ions or Sr ions. Otherwise need to investigate any possible phases formed during annealing.

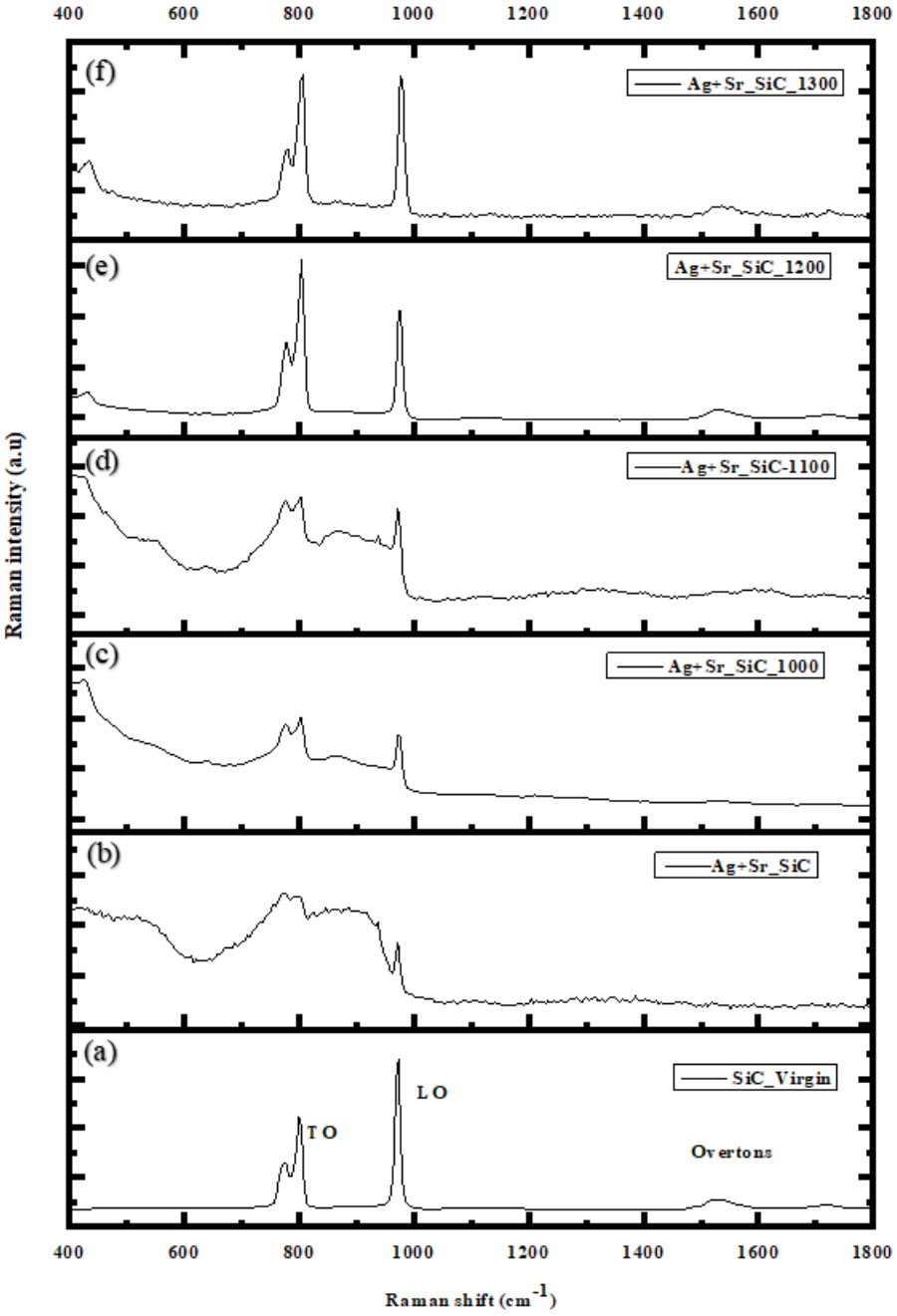

Figure 6. 2: *Raman spectra of a virgin SiC, silver and strontium co- implanted into SiC at a temperature of 600 ºC and after annealing from1000 ºC to 1300 ºC for 5 hours.*

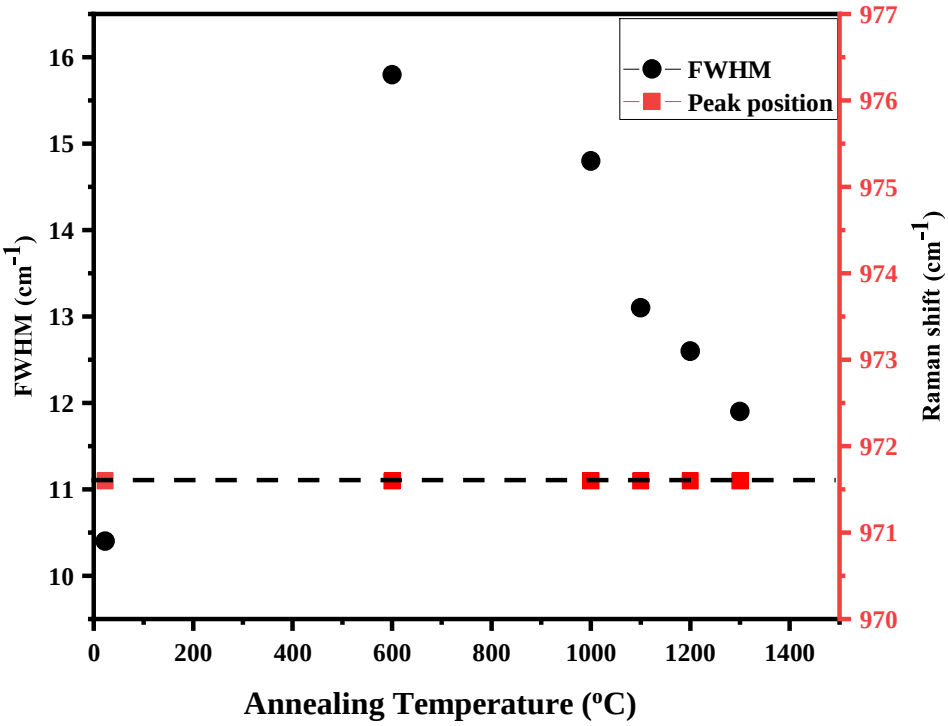

Figure 6. 3: *The peak position and FWHM of the LO peak as a function of temperature.*

6.1.3 SEM results

SEM micrographs of the virgin, co-implanted samples and annealed samples are shown in Fig. 6.4. The samples were isochronally annealed at temperatures ranging from 1000 °C to 1300 °C in steps of 100 °C for 5 hours. SEM micrograph of SiC-virgin has polishing marks on the surface as shown in Fig. 6.4 (a). These polishing marks are still visible but reduced in the as-implanted samples. The reduction of polishing marks is due to Ag and Sr bombarding the surface of the SiC causing some sputtering, while the visibility of polishing marks in the as-implanted samples indicates a lack of amorphization which is in consistent with the Raman results discussed earlier. Annealing at 1000 °C resulted in the appearance of grain boundaries in the surface (Fig. 6.4(c)). This indicates that a partial recrystallization occurred in the near surface of silicon carbide. The grain boundaries become more and more visible with the increase in the annealing temperature up to 1300 °C (Fig. 6.4(d), (e), and (f). Increasing the annealing temperature causes the sub-grain boundaries to decrease due to coarsening and thus the grain boundaries become visible [12]. Annealing at 1300 °C caused the appearance of pore openings on the grain boundaries as shown in Fi. 6.4 (f). These pore openings are where the bonds are weak. This is due to thermal etching which is more preferred on grain boundaries during heat treatment [9, 13].

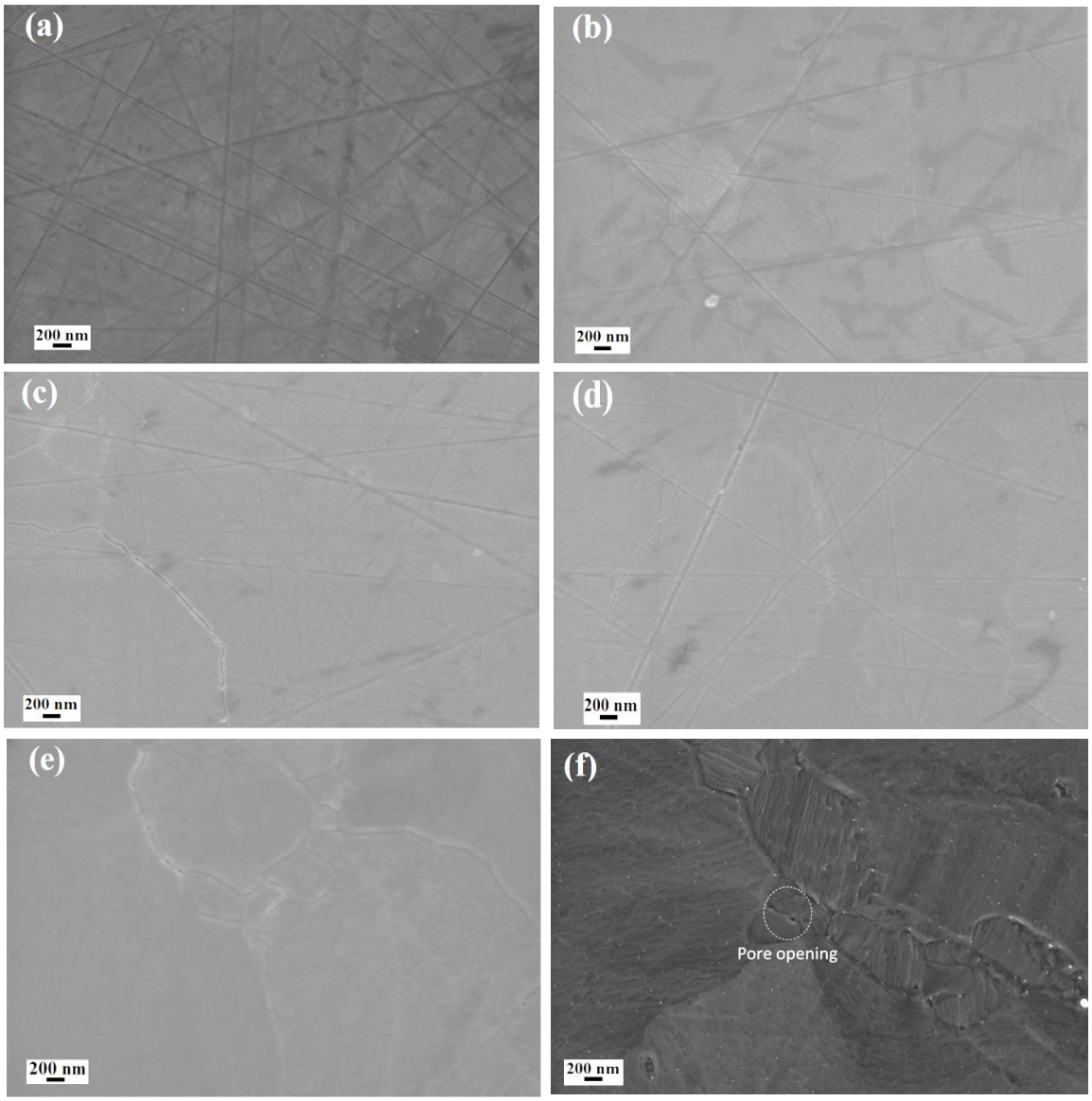

Figure 6. 4: *SEM micrographs of the virgin (a) co-implanted (b) and after isochronally annealed at, (c) 1000 ^{o}C, (d) 1100 ^{o}C, (e) 1200 ^{o}C, and (f) 1300 ^{o}C.*

6.1.4 Rutherford Backscattering Spectrometry (RBS) results

The migration of implanted fission product surrogates was monitored by Rutherford backscattering spectrometry (RBS) in the sample annealed at 1000 ^{o}C. Fig. 6.5 shows the RBS spectra of the as-implanted sample and sample annealed at 1000 ^{o}C. The as-implanted sample is included for comparison. From Fig. 6.5 the black spectrum is of the as-implanted sample and the red spectrum is for the sample annealed at 1000 ^{o}C. This insert shows the spectra of Ag &Sr in both samples. The arrows in Fig. 6.5 indicate surface positions of elements in energy channels. The profile of implants is asymmetric due to the overlapping of the implants. No change was detected in the sample implanted then annealed at 1000 ^{o}C indicating no migration

of implanted Ag and Sr after annealing at 1000 °C. These results agree with the previously reported results of Ag and Sr co-implanted into SiC then sequentially annealing up to 1000 ^{o}C [14].

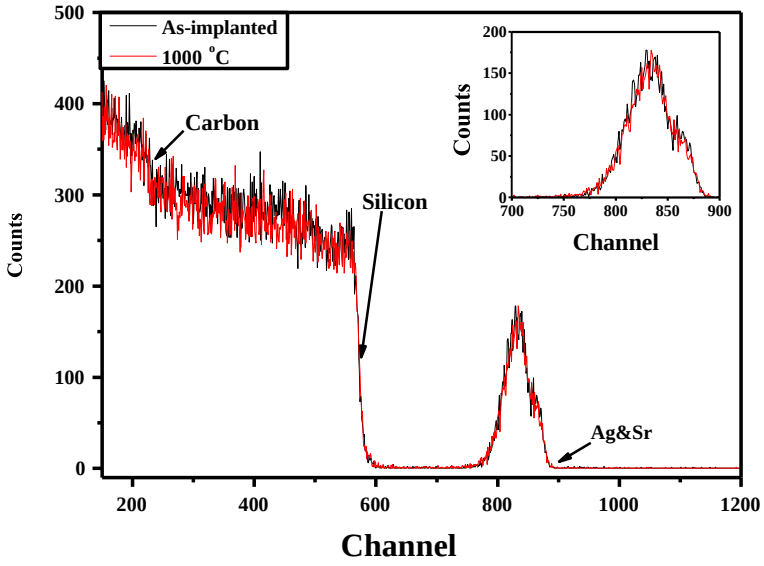

Figure 6. 5: *RBS spectra of Ag&Sr co- implanted into polycrystalline SiC at 600 ^{o}C before and after annealing at 1000 ^{o}C, with a an insert showing the zoomed Ag&Sr profiles.*

6.2 Ag, Sr, and He implants

6.2.1 Simulation results

Fig. 6.6 shows simulated depth profiles and displacement per atom (dpa) of Ag (360 keV), Sr (280 keV), and He ions (17 keV) implanted into SiC obtained using SRIM 2013[1]. Implantation resulted in a maximum dpa of 60 dpa and 45 dpa for Ag and Sr ions, respectively, at a depth of 90 nm below the surface. He ions produced a maximum dpa of 5.3 dpa at a depth of 110 nm below the surface. The total dpa of the three ions is 110 dpa at a depth of 85 nm below the surface. The Ag & Sr ions implantation resulted in the overlapping profiles with a projected range about 120 nm, and He ions implantation resulted in a projected range of around 130 nm. These observations allow investigation on the effect of He ions in the migration behaviour of Ag & Sr. The maximum total dpa retained by the triple implantation (Ag, Sr, He-

SiC) is higher than that retained by dual implantation (Ag&Sr-SiC). This indicates that triple implantation results in more damage retained.

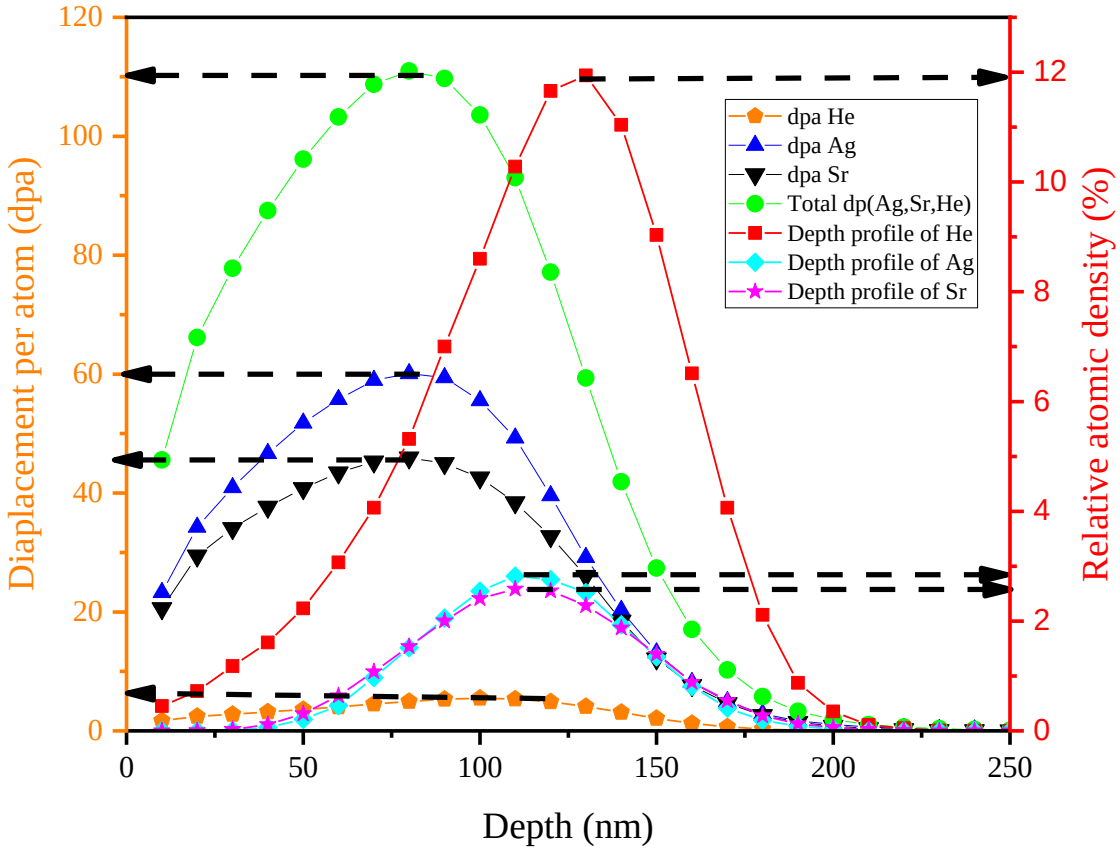

Figure 6. 6: *Simulated depth profiles and displacement per atom (dpa) of Ag (360 keV), Sr (280 keV), and He (17 keV) implanted into SiC.*

6.2.2 Raman results

Fig. 6.7 shows Raman spectroscopy results of Ag&Sr&He-SiC sample before and after isothermally annealing at temperatures ranging from 1000 ºC to 1300 °C in steps of 100 °C for 5 hours. Similar to the as implanted Ag&Sr-SiC sample, the as-implanted Raman spectrum bands became less intense after implantations as compared to the virgin ones. This indicates that the number of scattering molecules exposed to laser light was reduced, which is due to the highly disordered structure around the peak damage region [10]. Vacuum annealing at 1000 ºC already caused an increase in the LO mode indicating annealing of some defects. The intensity of LO mode increases with annealing temperature up to 1300 ºC. The main carbon bands D and

G were also clearly seen at this temperature. The appearance of carbon bands indicates the poor recrystallization of SiC owing to the presence of He. As can be seen from Fig. 6.7 and 6.8, the FWHM of peak LO increased to 15.2 cm^{-1} due to implantation, indicating poor crystallinity and the presence of defects.

Annealing the Ag&Sr&He-SiC at 1000 ^{o}C reduces the FWHM by 1.1 cm^{-1}, this indicates that there are less defects as compared to the as-implanted sample. With increasing annealing temperature, FWHM decreases, i.e. SiC crystallinity increases with the increase in annealing temperature. As a result of annealing up to 1300 ^{o}C, the FWHM reduced up to 11.50 cm^{-1}. Which is broader than that of a virgin, indicating some defects still present in the implanted SiC samples. As shown in Fig. 6.8, no changes in the LO mode could be observed after implantation and annealing up to 1300 ^{o}C. Therefore, the interatomic force for most of the atoms remains unchanged. Comparison of the Raman results of Ag & Sr-SiC and Ag & Sr & He-SiC samples, it is clear that the presence of He ions enhances recrystallization. Similar He ions enhanced recrystallization was reported in SiC co-implanted with He and Mg at RT annealed at 1573K. [15].

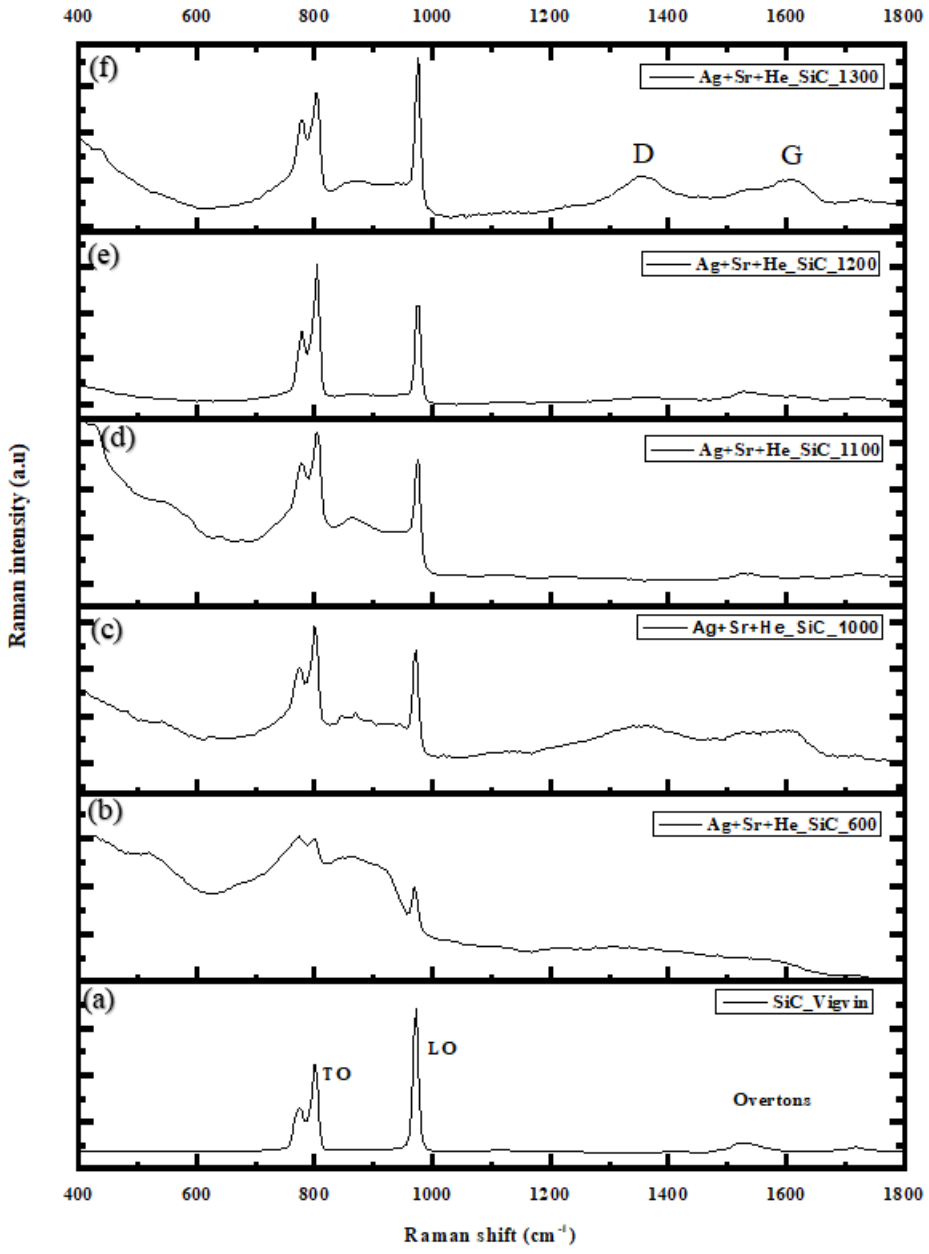

Figure 6. 7: *Raman spectra of virgin 3C-SiC and related sample implanted by Ag&Sr&He-SiC then annealed from 1000 °C to 1300 °C.*

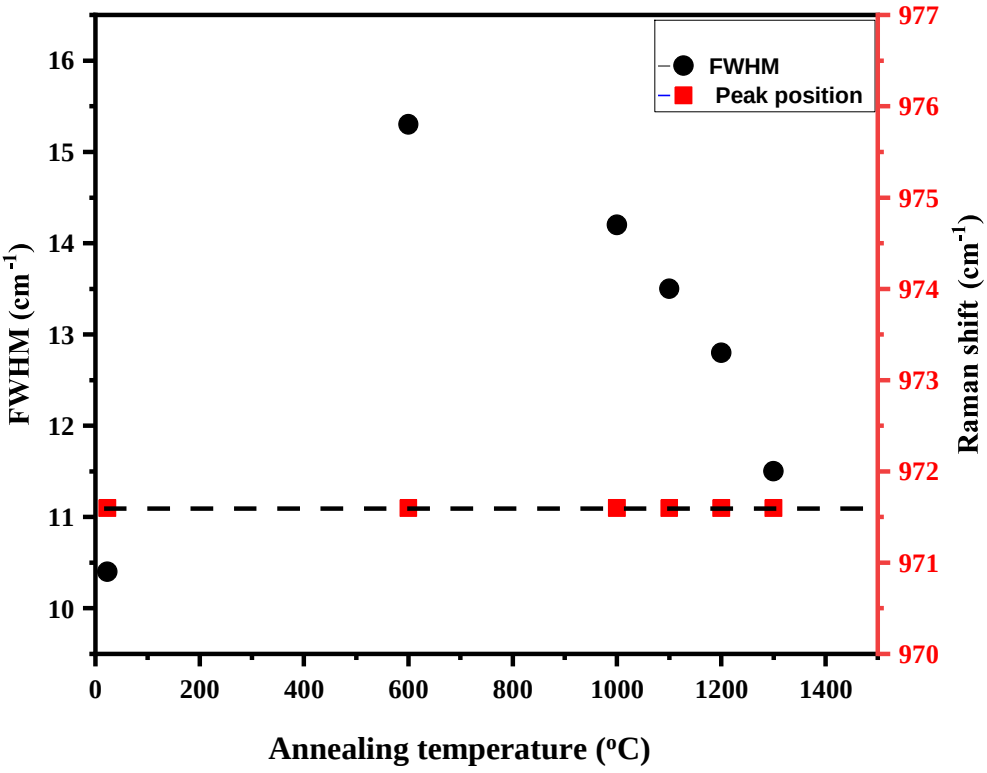

Figure 6. 8: *The FWHM and the peak position of the implanted sample Ag&Sr&He-SiC as a function of annealing temperature.*

6.2.3 Atomic Force microscope (AFM) results

To carefully investigate the surface morphology of Ag&Sr&He-SiC samples, before and after annealing, an Atomic Force microscope (AFM) was performed, and results are presented in Fig. 6.9. After the ion implantation, the sample in Fig. 6.9 (a) had some physical damages i.e. blisters and holes. Blisters are lighter in colour, while darker sports represent holes. The average height of blisters and cavities in nm before and after annealing is approximately 25.85 nm and -105,96 nm respectively. Interstitials and vacancies are present in the co-implanted samples i.e. in the Ag&Sr-SiC samples. In this study He ions of 17 keV were implanted in the Ag&Sr-SiC samples. As the implantation was done at high temperatures, the vacancies were mobile which increased the probability of Helium ions combining with other Helium ions to form bubbles. When bubbles form within the material, the high internal pressure in bubbles inside SiC results in deformation of the surface. As a result, blisters appear on the surface, which are light colour in AFM micrographs. Due to high pressure exerted by the largest bubble, the surface of the sample creaked, leading to exfoliation during implantation at higher temperature/annealing resulting in the appearance of holes on the surface. Hence the exfoliation of the surface increases

with increasing annealing temperature resulting in more holes on the surface as seen in Fig. 6.9. The out-diffusion of He results in the formation of cavities in the implanted SiC layers. Similar observations were reported by [7, 16].

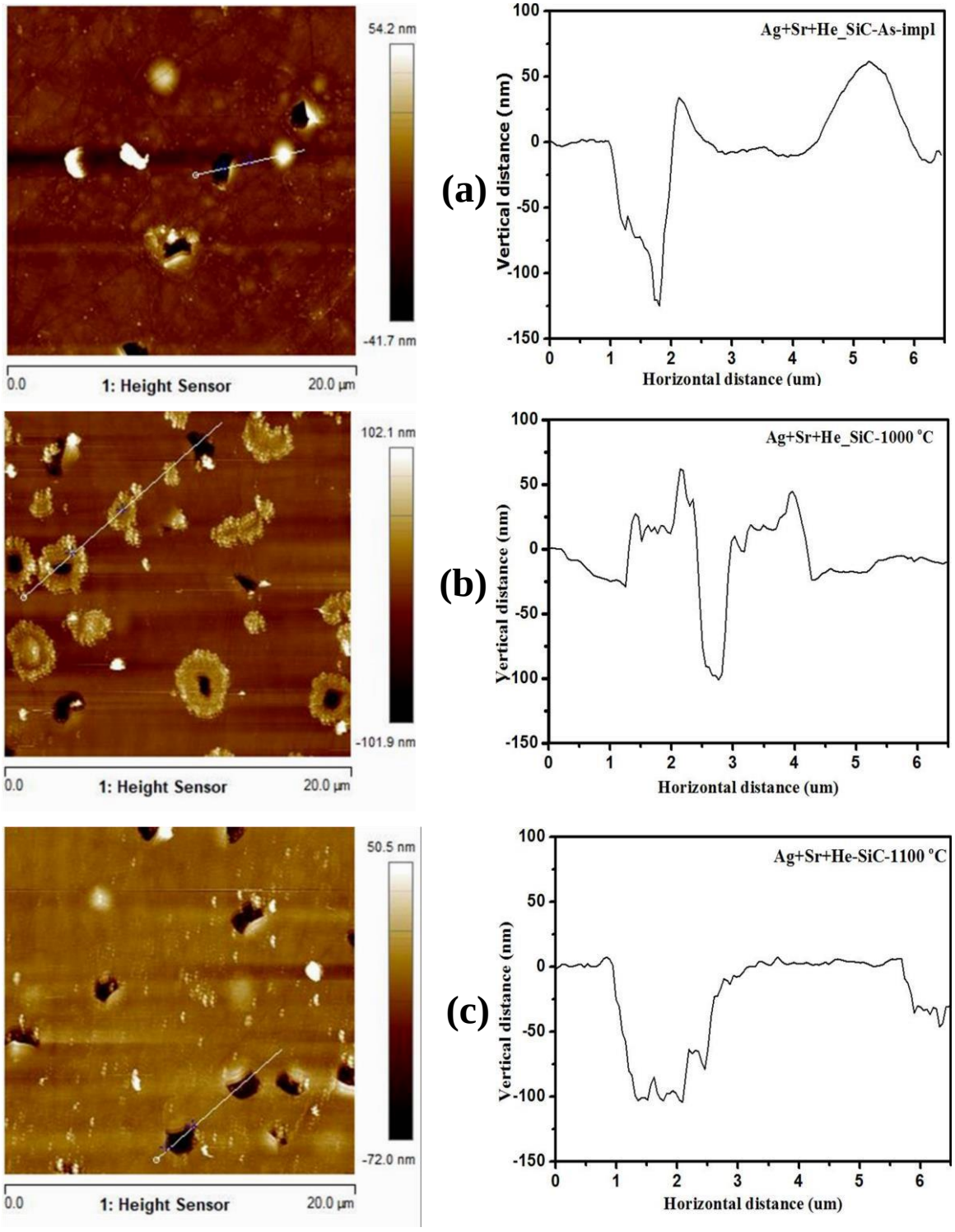

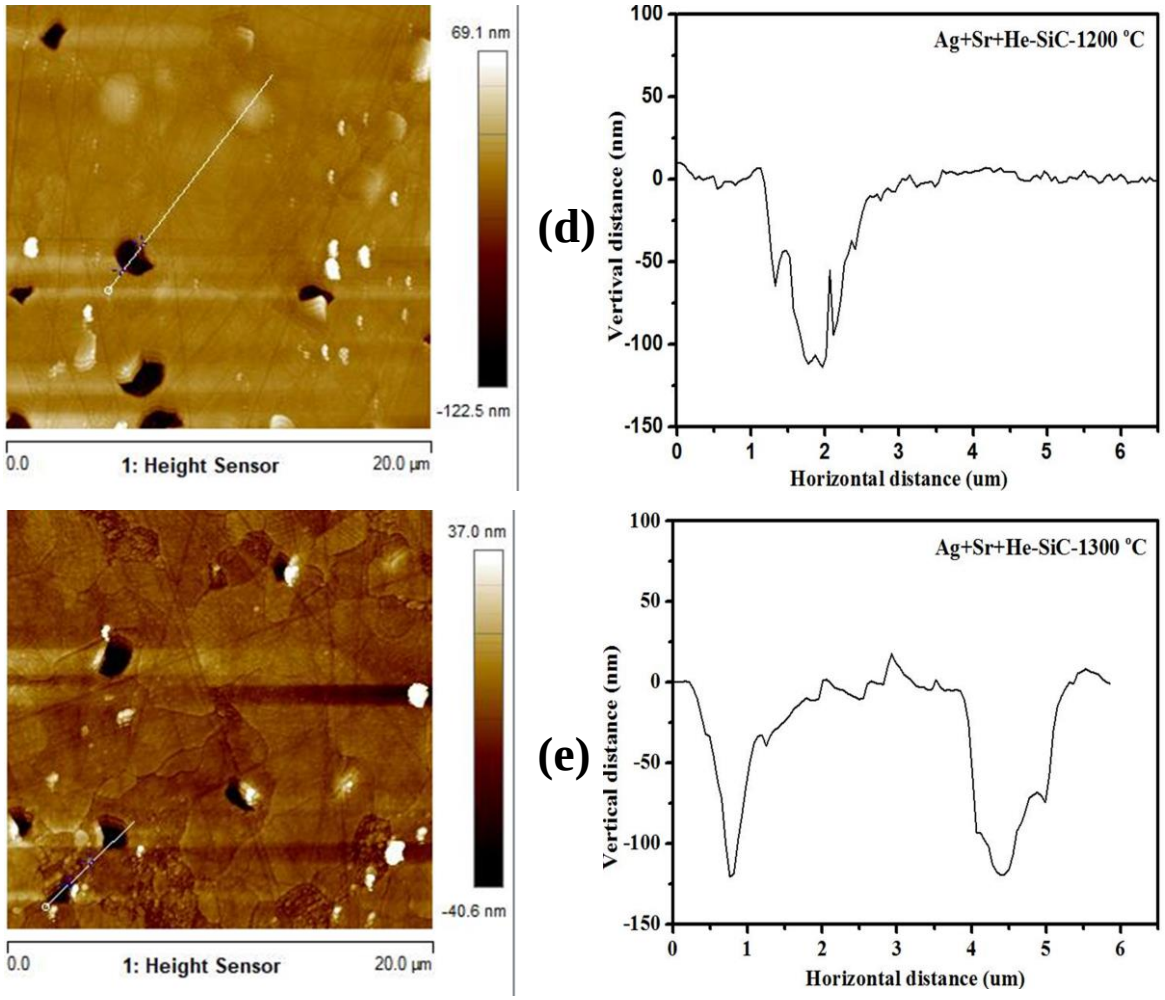

Figure 6. 9: *AFM 2D micrographs together with their line profiles of Ag&Sr&He-SiC before and after annealing at (b) 1000 °C, (c) 1100 °C, (d) 1200 °C, (e) 1300 °C.*

6.2.4 Heavy ion elastic recoil detector analyses (ERDA) results

Elastic recoil detection analysis (ERDA) was used to measure the depth profile of implanted species in both as-implanted and in the implanted then isochronally annealed at 1000 °C for 5 hours' sample. ERDA has an added advantage over RBS due to its ability of detecting He ions. As predicted by SRIM in Fig. 6.6, the Ag, Sr and He ions profiles are overlapping. Fig. 6.10 allowing the investigation of the effect of He ions in the migration behaviour of Ag and Sr. As expected for implanted profiles, the as-implanted Sr ions depth profile was almost Gaussian and symmetric, however the Ag profile consisted of double peak while the He ions profile is also

asymmetry with a prominent peak around 150 nm and shoulders around 65 and 280 nm. The double peak profile of Ag in the Ag and Sr co-implanted sample was found to be due to silver forming precipitates [14], while the asymmetric peak with 2 shoulders might be due to blisters and holes in the He implanted sample as shown in the AFM results. Since blisters are as the result of bubbles within the implanted region then the asymmetric peak with shoulder might be an indication of He forming bubbles in vacancies.

Implantation of He resulted in the migration of Ag and Sr towards the bulk and towards the surface. This migration towards the surface is more pronounced for Ag and is accompanied by the Ag profile having the main peak at 96 nm and the small peak at 42 nm. While Sr profile has a peak around 65 nm. From SRIM predictions, the main peak Sr and Ag main peaks are located in relatively highly defective region while the small Ag peak is at the less defective surface region. He needs vacancies to form bubbles and the AFM results showed that the He implanted samples have bubbles and holes. The formation of holes are the results of high He implantation temperature which resulted in the some out diffusion of He leaving holes or cavities in the implanted regions which are responsible of trapping both implanted Ag and Sr. Annealing at 1000 ^{o}C caused further migration of the implanted Ag and Sr towards the bulk and the surface. The migration of Sr was accompanied by the formation of double peak profile with a prominent peak around 41 nm and the main one around 130 nm. The migration of Ag was characterized by Ag profile with a prominent peak around 105 nm and a shoulder around 205 nm.

The He ions profile from the annealed sample also has a prominent peak around 156 nm and 4 nm with a shoulder 262 nm. From these results, it is quite clear that after annealing the prominent peaks appeared in the region with high defects and relatively low He ions concentration indicating the trapping of implanted species by holes or cavities. Since the migration of implanted species was not seen in the Ag and Sr co-implanted samples after annealing at 1000 ^{o}C, it seems He bubbles enhance migration while cavities trap the implanted species. To get more insight in the role of He in the migration of Ag and Sr needs to be investigated at elevated temperatures and during isothermal annealing. Moreover, the migration of Ag and Sr needs to be investigated at an atomic scale using transmission electron microscopy (TEM).

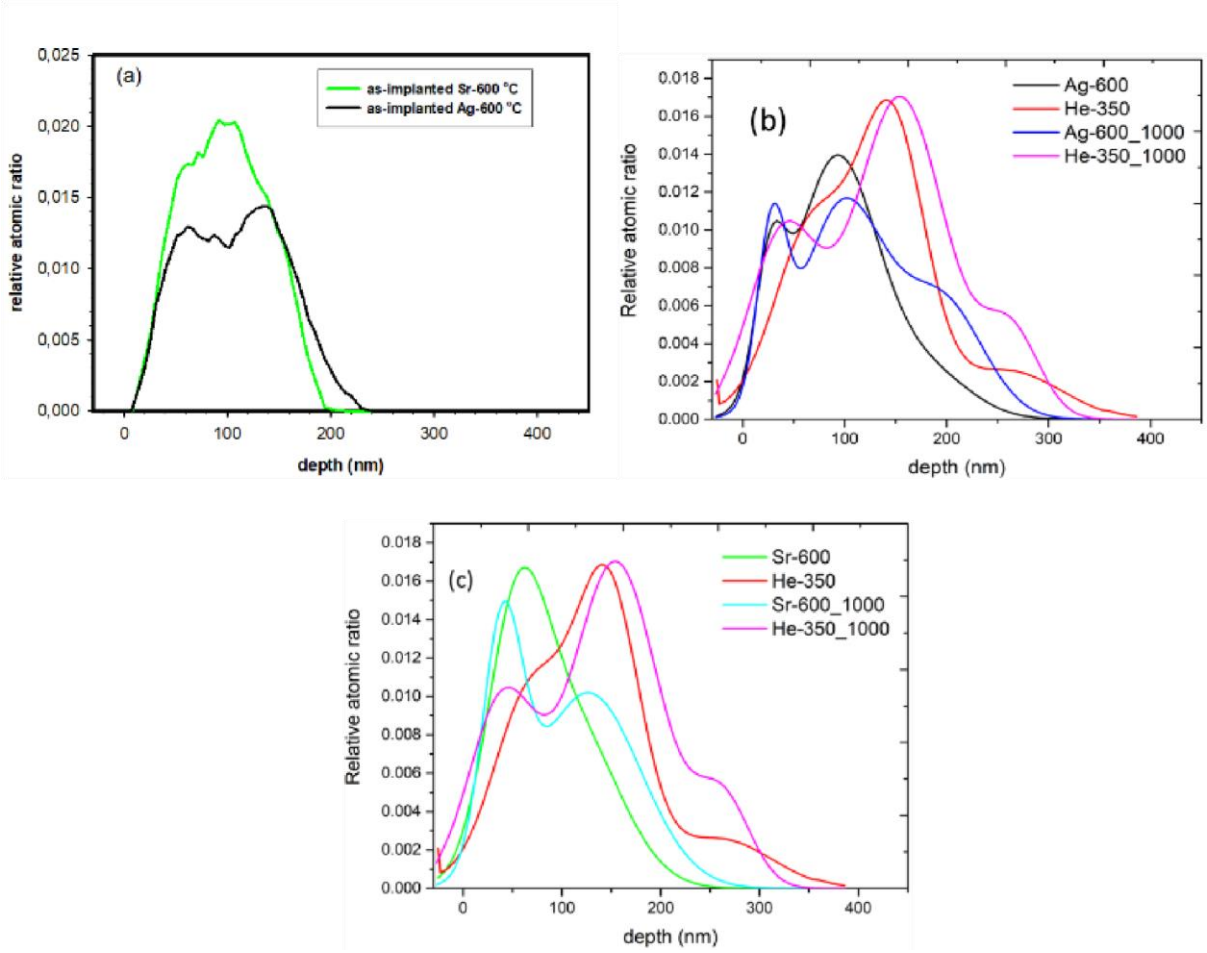

Figure 6.10: *ERDA depth profiles of Ag&Sr&He implanted into polycrystalline SiC before and after annealing at 1000 °C for 5 hours.*

References

1. Ziegler, J. F., Ziegler, M. D., & Biersack, J. P. (2010). SRIM–The stopping and range of ions in matter (2010). Nuclear Instruments and Methods in Physics Research Section B: Beam Interactions with Materials and Atoms, 268(11-12), 1818-1823.
2. Devanathan, R., Weber, W. J., & Gao, F. (2001). Atomic scale simulation of defect production in irradiated 3C-SiC. Journal of Applied Physics, 90(5), 2303-2309.
3. Hlatshwayo, T. T., Sebitla, L. D., Njoroge, E. G., Mlambo, M., & Malherbe, J. B. (2017). Annealing effects on the migration of ion-implanted cadmium in glassy carbon. Nuclear Instruments and Methods in Physics Research Section B: Beam Interactions with Materials and Atoms, 395, 34-38.
4. Gao, F., & Weber, W. J. (2002). Cascade overlap and amorphization in 3C− SiC: Defect accumulation, topological features, and disordering. Physical review B, 66(2), 024106.
5. Malherbe, J. B., Van Der Berg, N. G., Kuhudzai, R. J., Hlatshwayo, T. T., Thabethe, T. T., Odutemowo, O. S., & Wendler, E. (2015). Scanning electron microscopy of the surfaces of ion implanted SiC. Nuclear Instruments and Methods in Physics Research Section B: Beam Interactions with Materials and Atoms, 354, 23-27.
6. Abdelbagi, H. A. A., Skuratov, V. A., Motloung, S. V., Njoroge, E. G., Mlambo, M., Hlatshwayo, T. T., & Malherbe, J. B. (2019). Effect of swift heavy ions irradiation on the migration behaviour of strontium implanted into polycrystalline SiC. Nuclear Instruments and Methods in Physics Research Section B: Beam Interactions with Materials and Atoms, 451, 113-121.
7. Hlatshwayo, T. T., Maepa, C. E., Msimanga, M., Mlambo, M., Njoroge, E. G., Skuratov, V. A., & Malherbe, J. B. (2021). Helium assisted migration of silver implanted into SiC. Vacuum, 183, 109865.
8. Wang, X., Zhang, Y., Liu, S., & Zhao, Z. (2014). Depth profiling by Raman spectroscopy of high-energy ion irradiated silicon carbide. Nuclear Instruments and Methods in Physics Research Section B: Beam Interactions with Materials and Atoms, 319, 55-61.
9. Abdalla, Z. A. Y., Ismail, M. Y. A., Njoroge, E. G., Wendler, E., Malherbe, J. B., & Hlatshwayo, T. T. (2021). Effect of heat treatment on the migration behaviour of selenium implanted into polycrystalline SiC. Nuclear Instruments and Methods in Physics Research Section B: Beam Interactions with Materials and Atoms, 487, 30-37.

10. Xu, Z., He, Z., Song, Y., Fu, X., Rommel, M., Luo, X., & Fang, F. (2018). Topic review: Application of Raman spectroscopy characterization in micro/nanomachining. Micromachines, 9(7), 361.
11. Abdalla, Z. A. Y., Ismail, M. Y. A., Njoroge, E. G., Hlatshwayo, T. T., Wendler, E., & Malherbe, J. B. (2020). Migration behaviour of selenium implanted into polycrystalline 3C–SiC. Vacuum, 175, 109235.
12. Sheng, H., Sun, Z., Uytdenhouwen, I., Van Oost, G., & Vleugels, J. (2015). Temperature and deformation effect on the low and high angle grain boundary structure of a double forged pure tungsten. International Journal of Refractory Metals and Hard Materials, 50, 184-190.
13. Van der Berg, N. G., Malherbe, J. B., Botha, A. J., & Friedland, E. (2012). Thermal etching of SiC. Applied surface science, 258(15), 5561-5566.
14. Hlatshwayo, T. T., Mtshonisi, N., Njoroge, E. G., Mlambo, M., Msimanga, M., Skuratov, V. A., Motloung, S. V. (2020). Effects of Ag and Sr dual ions implanted into SiC. Nuclear Instruments and Methods in Physics Research Section B: Beam Interactions with Materials and Atoms, 472, 7-13.
15. Liu, M., Gong, H., Liu, W., Liu, R., & Cao, J. (2021). Effects of He on the recrystallization and Mg diffusion in Mg ion implanted CVD-SiC. Journal of Nuclear Materials, 545, 152747.
16. Beaufort, M. F., Pailloux, F., Declémy, A., & Barbot, J. F. (2003). Transmission electron microscopy investigations of damage induced by high energy helium implantation in 4H–SiC. Journal of applied physics, 94(11), 7116-7120.

Chapter 7

Conclusions and future studies

In this study, the effect of He ions on the migration behavior of Ag and Sr co-implanted into SiC was investigated. Ag ions of 360 keV were implanted into polycrystalline SiC to a fluence of 2×10^{16} cm^{-2} at 600 ^{o}C. On the same samples, Sr ions of 280 keV were also implanted to a fluence of 2×10^{16} cm^{-2} at 600 ^{o}C. Some of the co-implanted samples were implanted with 17 keV He to a fluence of 1×10^{17} cm^{-2} at 350 ^{o}C. The implanted samples were then isochronally annealed at a temperature ranging from 1000 ^{o}C to 1300 ^{o}C. Raman spectroscopy and scanning electron microscopy (SEM) were used to investigate structural and morphological changes of the samples. Atomic force microscopy (AFM) was used to measure the changes in the surface topography and roughness. Rutherford backscattering spectrometry (RBS) and elastic recoil detection analyses (ERDA) were used to monitor the migration behaviour of the implanted samples.

The Raman results of Ag&Sr-SiC and Ag&Sr&He-SiC samples showed that implantation caused the accumulation of defects without amorphization of the SiC structure. In both samples, isochronal annealing resulted in healing or annealing out of defects. This annealing of defects progressed with increase in annealing temperature up to 1300 ^{o}C. However, the total annealing of defects was not achieved. SEM micrograph of SiC-virgin showed polishing marks on the surface. These polishing marks became less obvious and reduced in the implanted samples indicating a lack of amorphization which is in agreement with the Raman results**.** Annealing at 1000 ^{o}C resulted in the appearance of grain boundaries in the surface indicating the partial recrystallization in the near-surface of silicon carbide. The grain boundaries become more visible with the increase in the annealing temperature up to 1300 ^{o}C. Annealing at 1300°C also caused pore openings to appear on the grain boundaries. The RBS results of the Ag and Sr co-implanted sample showed no migration of the implanted species after annealing at 1000 ^{o}C. AFM results showed that implantation of He resulted in the formation of blisters and holes on the surface, indicating the production of He bubbles in SiC that ejected He during implantation, leaving some cavities on the surface. Due to high pressure exerted by the largest bubble. The surface of the sample cracked leading to exfoliation during implantation at higher temperature/annealing resulting in the appearance of holes on the surface. The exfoliation of the surface increased with increasing annealing temperature resulting in more holes on the surface. The ERDA profiles showed that implantation of He resulted in the migration of Ag and

Sr towards the bulk and towards the surface. This migration towards the surface was more pronounced for Ag. The formation of holes are the results of high He implantation temperature which resulted in the some out diffusion of He leaving holes or cavities in the implanted regions which are responsible of trapping both implanted Ag and Sr. Annealing at 1000 ^{o}C caused further migration of the implanted Ag and Sr towards the bulk and the surface. Since the migration of implanted species was not seen in the Ag and Sr co-implanted samples after annealing at 1000 ^{o}C, it seems He bubbles enhance migration while cavities trap the implanted species.

The results of this study demonstrate the role of He in the migration of Ag and Sr implanted into SiC and are crucial in understanding the release of different FPs in a TRISO particle where SiC is used as the main FPs diffusion barrier. In a TRISO particle, FPs co-exist in the presence of He. However, to get more insight into the role of He in the migration of Ag and Sr in SiC, isochronal annealing studies need to be performed at elevated temperatures to accommodate the accidental conditions and isothermal annealing studies need to be performed for prolonged periods to mimic the operation of nuclear reactors. Moreover, the migration of Ag and Sr needs to be investigated at an atomic scale using transmission electron microscopy (TEM) and some modelling.